Microphysics of Maritime Tropical Convective Updrafts at Temperatures from −20° to −60°C

ANDREW J. HEYMSFIELD AND AARON BANSEMER

National Center for Atmospheric Research, Boulder, Colorado*

GERALD HEYMSFIELD

NASA GSFC, Greenbelt, Maryland

ALEXANDRE O. FIERRO

NOAA/Hurricane Research Division, Atlantic Oceanographic Meteorological Laboratory, Miami, Florida

(Manuscript received 17 February 2009, in final form 25 June 2009)

ABSTRACT

Anvils produced by vigorous tropical convection contribute significantly to the earth's radiation balance, and their radiative properties depend largely on the concentrations and sizes of the ice particles that form them. These microphysical properties are determined to an important extent by the fate of supercooled droplets, with diameters from 3 to about 20 microns, lofted in the updrafts. The present study addresses the question of whether most or all of these droplets are captured by ice particles or if they remain uncollected until arriving at the −38°C level where they freeze by homogeneous nucleation, producing high concentrations of very small ice particles that can persist and dominate the albedo.

Aircraft data of ice particle and water droplet size distributions from seven field campaigns at latitudes from 25°N to 11°S are combined with a numerical model in order to examine the conditions under which significant numbers of supercooled water droplets can be lofted to the homogeneous nucleation level. Microphysical data were collected in pristine to heavily dust-laden maritime environments, isolated convective updrafts, and tropical cyclone updrafts with peak velocities reaching 25 m s^{-1}. The cumulative horizontal distance of in-cloud sampling at temperatures of −20°C and below exceeds 50 000 km. Analysis reveals that most of the condensate in these convective updrafts is removed before reaching the −20°C level, and the total condensate continues to diminish linearly upward. The amount of condensate in small (<50 μm in diameter) droplets and ice particles, however, increases upward, suggesting new droplet activation with an appreciable radiative impact. Conditions promoting the generation of large numbers of small ice particles through homogeneous ice nucleation include high concentrations of cloud condensation nuclei (sometimes from dust), removal of most of the water substance between cloud base and the −38°C levels, and acceleration of the updrafts at mid- and upper levels such that velocities exceed 5–7 m s^{-1}.

1. Introduction

Cirrus clouds at a given time cover about 20% of tropical latitudes and contribute significantly to regional and global radiation budgets (Rossow and Schiffer 1999). Optically thick tropical cirrus are produced primarily through deep convection and generate as much as 25% of the earth's net cloud radiative forcing (Hartmann et al. 1992). The primary impact of thin versus thick cirrus is on the shortwave energy budget, and the albedo of these ice clouds depends on their formation processes. The albedo is influenced by the environment in which the deep convection forms and depends critically on the number concentration of very small ice particles. One little-explored aspect of the formation of optically thick anvil cirrus lies in the role of dust. Recent investigations have noted the relationship between African dust and tropical cyclone activity (Evan et al. 2006; Dunion and Velden 2004; Wong and Dessler 2005). Our

* The National Center for Atmospheric Research is sponsored by the National Science Foundation.

Corresponding author address: Andrew Heymsfield, NCAR, P.O. Box 3000, Boulder, CO 80307.
E-mail: heyms1@ncar.ucar.edu

DOI: 10.1175/2009JAS3107.1

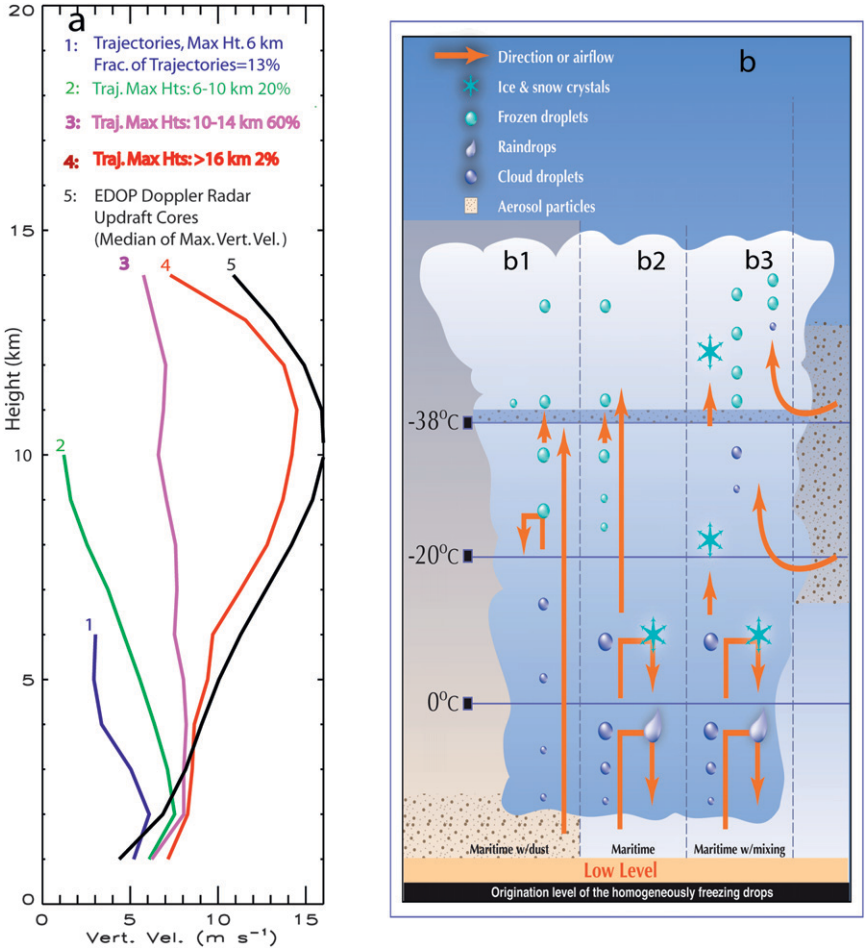

FIG. 1. (a) Vertical profiles of vertical velocities from simulations of a vigorous maritime squall line observed during the Tropical Ocean and Global Atmosphere Coupled Ocean–Atmosphere Response Experiment (TOGA COARE) (after Fierro et al. 2009). Curve 1 shows parcels that do not reach 6 km; curve 2, those reaching 6 to 10 km; curve 3, 10–14 km; and curve 4, >14 km. Fraction of parcels reaching the different heights are shown at the top of the panel. Curve 5 shows median values of peak vertical velocities derived for low-latitude, vigorous, deep convective clouds from the NASA ER-2 Doppler radar (EDOP) measurements during 10 field campaigns (Heymsfield et al. 2010). (b) Schematic depiction of the evolution of hydrometeors in maritime convective updrafts for three scenarios: b1, dust in the inflow; b2: clean conditions; and b3, entrainment of dust at midlevels. Freezing of the droplets homogeneously occurs in the shaded area near −38°C.

investigation uses both new and existing observations to characterize microphysical properties within the highly supercooled and overlying regions of tropical maritime deep convection, including cases in which low-level dust was entrained into the convective core. The focus in this paper is on the exploration of the microphysical properties and processes relevant to the −20 to −60°C temperature range of deep maritime tropical convection. Such regions cover 3% of the tropics directly, with a much larger percentage when considering the cirrostratus they generate (see Rossow and Schiffer 1999).

The following outlines some dominant microphysical processes operating in vigorous tropical oceanic and continentally perturbed oceanic deep convective cloud systems with peak updrafts exceeding 10 m s^{-1} (see our Fig. 1 and also Stith et al. 2004). Individual parcels of those updrafts can be transported from the boundary layer to near the tropopause (Fig. 1a, curves 4 and 5), although most parcels of an intense convective core only reach midlevels (Fig. 1a, curves 2 and 3). Between cloud base and the 0°C temperature (T) level is a deep layer with warm rain processes (Fig. 1b, zones b2 and b3). The condensate made available by the updraft forms cloud

droplets on cloud condensation nuclei (CCN). Dust in the boundary layer may contain soluble material and act as CCN to produce cloud droplets (Twohy et al. 2009; see also Fig. 1, zone b1). Drops develop by coalescence as the rain distributions develop. A fraction of the large drops falls out through the updrafts because the peak updrafts warmer than 0°C are in the mean less than 7 m s^{-1} (Zipser and LeMone 1980; Zipser et al. 1981; Lucas et al. 1994; Fierro et al. 2009; Heymsfield et al. 2010) and are of the same order as the terminal velocities of the drops larger than about 1 mm. Condensation feeds the cloud droplet spectrum; large raindrops grow chiefly by collision–coalescence, while some either fall out or break up from drop–drop collisions. The updraft parcel accelerates because of partial unloading of the large drops (Fig. 1a, curve 5; Samsury and Zipser 1995; May and Rajopadhyaya 1996). There is appreciable entrainment in the first few kilometers above cloud base (e.g., Zipser 2003; Murata and Ueno 2005; Fierro et al. 2009), supporting the notion that undiluted towers are rare.

Updraft parcels arrive at 0°C with small to medium-sized raindrops and substantial concentrations of smaller cloud droplets (<100 μm), sustained by the condensation from the updraft and collisional breakup. As temperatures decrease from 0°C to about −10°C and updrafts exceed 5 m s^{-1} (Heymsfield et al. 2010), growth of the supercooled droplets and unfrozen drops is sustained, and condensational and accretional growth initiates on frozen rain, graupel, and pristine ice (Stith et al. 2004). An exception may occur in Atlantic hurricanes, where liquid water appears to be mostly confined to temperatures of −5°C and warmer (Black and Hallett 1986, 1999). However, intense Atlantic hurricane updrafts such as found for Emily (1987) are likely to contain liquid water to temperatures much below −5°C (Black et al. 1994). In tropical convection, the frozen drops briefly undergo growth as a water and ice mixture and then grow as dry graupel as they are lofted and cool. They accrete cloud droplets, and their fall velocities increase. By −10°C, concentrations of heterogeneously nucleated ice and ice crystals produced by secondary processes begin to become appreciable (Hallett and Mossop 1974).With updrafts below about 10 m s^{-1}, corresponding to the fall speeds of 5–10 mm diameter graupel of solid ice density, the larger graupel fall through or out of the updrafts. Pristine ice crystals grow while being lofted to a size where they accrete supercooled liquid water (LW). The concentrations of ice crystals produced from ice nuclei continue to increase as the temperature decreases (Meyers et al. 1992). At temperatures colder than about −17°C, most droplets and drops of all sizes freeze or are accreted, and ice growth is primarily through vapor diffusion and aggregation (Stith et al. 2004). Entrainment of midtropospheric aerosols and their activation to cloud particles in the updrafts may be a significant process occurring in the upper parts of the updrafts (Fridlind et al. 2004; see our Fig. 1b, zone b3). In hurricane updrafts, the microphysical processes can differ because of appreciable azimuthal transport and vertical recycling of the hydrometeors (Marks and Houze 1984).

The central question we address here is this: Under what conditions will a portion of the cloud droplet concentration transported upward in updrafts avoid being accreted and/or evaporated by the growing ice particle population before reaching the level of −38°C where droplet freezing occurs spontaneously? Why is this issue important? First, what happens in the supercooled region (where liquid water exists at temperatures <0°C) depends strongly on how much condensate reaches that level relative to how much falls out—a question that is basic to the understanding of precipitation processes at work in convection. Second, there is the potential effect on the cloud albedo. Consider a population of 15-μm-diameter droplets collocated with a population of 1-mm-diameter graupel lofting in an updraft at a temperature of −20°C. Simple calculations involving realistic liquid and ice water contents (LWC and IWC, respectively) show that whether the droplets are collected by the ice or remain uncollected until reaching the homogeneous nucleation level can have a profound effect on the radiative properties of a tropical maritime convective cloud.

If droplets are transported to temperatures below −38°C, they freeze by homogeneous nucleation, producing high concentrations of ice particles. Here, high concentrations are subjectively quantified as being much larger than expected for heterogeneous or secondary ice nucleation processes at a temperature of −38°C and of the same order of magnitude as the concentrations of droplets activated at cloud base for the given aerosol loading and vertical velocities: for maritime convection, >10 cm^{-3}, and for continentally influenced convection, >100 cm^{-3}. The homogeneous ice nucleation process depends on the temperature and the droplet volume and purity (e.g., Koop et al. 2000). Rosenfeld and Woodley (2000) reported in situ measurements in Texas deep convective clouds with vigorous updrafts. With the high concentrations of cloud droplets typical of continental clouds, their results suggest that most of the condensed water in the sampled updrafts remained liquid down to almost −38°C. Freezing occurred rapidly at slightly lower temperatures. In tropical maritime clouds, drops originating at cloud base are less likely to survive to the −38°C level because fewer but larger droplets and drops and weaker updrafts allow much of the condensate to fall

out through the updrafts. An exception for low-latitude clouds is for vigorous convection, where supercooled liquid water can be sustained to temperatures required for homogeneous nucleation (Heymsfield et al. 2005).

Using new observations and reanalyzing earlier ones, our study takes a more comprehensive look at the microphysical properties and processes operating in vigorous tropical maritime updrafts and surrounding regions at temperatures from −20° to −60°C. Peak updraft velocities are higher than those lower down in the cloud (see Fig. 1a, curve 5) and in the mean increase through this temperature range, with higher values noted for generic convection than for tropical cyclones (Heymsfield et al. 2010). Section 2 provides an overview of the data and instruments, and section 3 presents the observations. The results are discussed in section 4, and conclusions are drawn in section 5.

2. Data

a. Field campaigns

The data used here come from seven field programs conducted over the past decade primarily in low-latitude locations, favoring those cases with strong convection (Program acronyms are listed in Table 1.) Field programs include three National Aeronautics and Space Administration (NASA) Tropical Rain Measuring Mission (TRMM) campaigns with twenty-five flights over the Gulf of Mexico [TRMM Texas–Florida Underflights (TEFLUN-B), August–September 1998]; in Rondonia, Brazil [TRMM Large-Scale Biosphere–Atmosphere Experiment in Amazonia (LBA), January and February 1999]; and in Kwajalein, Marshall Islands [TRMM Kwajalein Experiment (KWAJEX), August and September 1999]. Microphysical properties and updraft statistics during two of the TRMM campaigns have been presented by Stith et al. (2004) and Anderson et al. (2005). Data used in our analysis were also collected over the western Caribbean in Hurricanes Erin and Humberto [Fourth NASA Convection and Moisture Experiment (CAMEX-4), September 2001]. Observations from Humberto are reported in Heymsfield et al. (2006). An intense convective core was sampled along a sea breeze front in southeastern Florida during the Cirrus Regional Study of Tropical Anvils and Cirrus Layers–Florida-Area Cirrus Experiment (CRYSTAL-FACE, hereafter C-F), July 2002]. Liquid droplets at a temperature of −34°C and high concentrations of presumably homogeneously nucleated particles were detected at higher, colder levels of the cloud (Heymsfield et al. 2005). We further interpret those data here. During C-F, a second aircraft sampled nine clouds near the tops of anvils. Near Darwin, Australia, sampling was conducted in the upper parts of four ''Hector'' storms, in three deep-layer clouds associated with monsoon convection, and in two squall lines [Aerosol and Chemical Transport in Tropical Convection Experiment (ACTIVE), December 2005–February 2006]. Hector storms are the name given to intense convection that forms most days in the period leading up and during the wet season near Melville Island (north of Darwin). Details of the goals and flights from that field program are discussed in Vaughan et al. (2008). Most recently, data were collected in and around dust associated with the Saharan air layer (SAL) on thirteen days west and south of Cape Verde, Africa [during the NASA African Monsoon Multidisciplinary Analyses (NAMMA) in 2006]. Storms were penetrated on two days. One of these (20 August) became Tropical Storm Debby the day after it was sampled and the second (12 September) developed into Hurricane Helene. Zipser et al. (2009) summarize the NAMMA experiment and preliminary observations and Twohy et al. (2009) report on microphysical observations in the low-level clouds that were influenced by dust.

b. Instruments

For TRMM and C-F, supercooled liquid water was detected using a Rosemount Icing (RICE) probe. The RICE calibration uses a theoretically based method involving the sublimation of ice from the RICE probe following passage through a liquid water cloud (Mazin et al. 2001), and we are confident that a liquid water content of 0.02 g m^{-3} and above can be detected and quantified. Measurements from laser diode hygrometers, evaluated and validated in known regions near water saturation (containing cloud water) and near ice saturation (in contrails near −50°C), are used in interpreting the C-F and NAMMA data.

Our analysis considers particle size distributions (PSDs) acquired with a 2D-C and CIP, 2D-P and an HVPS probe. (Probe acronyms and size ranges are given in Table 1.) The PSDs cover the particle diameter range from a minimum of about 75–125 μm (depending on the probe used and the aircraft true airspeed) to 1 cm and larger. The 2D probe data have been processed objectively to remove artifacts produced by shattering on the probes' leading edges (see Field et al. 2006). It was desirable to average the 2D probe data over 5-s intervals to ensure that sufficient numbers of particles 1 mm and above, normally present in low concentrations, were obtained. An analysis of the sampling statistics for the 2D probe data is reported elsewhere (Heymsfield et al. 2008) and therefore will not be repeated here.

The PSDs of small particles, defined here as those with diameters from 3 to 50 μm, were acquired with forward scattering spectrometer probes (FSSPs) and cloud and

TABLE 1. List of acronyms and variables.

Acronym	Name
Figure captions	
2D-C	PMS two-dimensional imaging probe, sizing from about 100 μm to >2 mm
2D-P	PMS two-dimensional imaging probe, sizing from about 400 μm to >6 mm
A_{2D}	Cross-sectional area in sizes measured by 2D probe, derived from particle images and PSD
A_s	Cross-sectional area derived from FSSP or CAS PSD, assuming particles are solid ice spheres
ACTIVE	Aerosol and Chemical Transport in Tropical Convection Experiment
c_m	Coefficients relating $IWC_{FSSP,CAS}$ to IWC_{2D}
C	Ice crystal shape factor
CAMEX-4	Fourth NASA Convection and Moisture Experiment
CAS	DMT Cloud and Aerosol Spectrometer, sizing from about 0.5–50 μm
CCN	Cloud condensation nuclei
CIP	DMT Cloud Imaging Probe (CIP), sizing from about 100 to 2000 μm
c_m, c_a	Coefficients that relate IWC or A in FSSP or CAS sizes to those in 2D probe sizes
CRYSTAL-FACE (C-F)	Cirrus Regional Study of Tropical Anvils and Cirrus Layers (CRYSTAL)-Florida Area Cirrus Experiment (FACE)
CVI	Counterflow Virtual Impactor probe
CWC	Condensed (liquid + ice) water content
dm/dt	Mass growth rates
DMT	Droplet Measurement Technologies
F	Ventilation coefficient for ice crystal
FSSP	PMS Forward Scattering Spectrometer Probe, sizing from about 3–50 μm
G_i', G_w'	Ice particle diffusional growth rate and droplet condensational growth rate parameters
HVPS	SPEC High Volume Precipitation Spectrometer, sizing from about 200 μm to 6 cm
IWC	Ice water content
IWC_{2D}	IWC in sizes measured by 2D probe, derived from PSD
IWC*s*	IWC derived from FSSP or CAS PSD, assuming particles are solid ice spheres
KWAJEX	TRMM Kwajalein Experiment
λ	Slope of exponential particle size distribution
LASE	The Lidar Atmospheric Sensing Experiment instrument
LBA	TRMM Large-Scale Biosphere–Atmosphere Experiment in Amazonia
LW	Liquid water
LWC	Liquid water content
m	Ice crystal mass
NAMMA	NASA African Monsoon Multidisciplinary Analyses
N_0	Intercept parameter of exponential particle size distribution
N_s	Total concentration of small (<50 μm) particles
RH, RH_w, RH_i	Relative humidity with respect to water, water, ice
PSD	Particle size distribution
ρ_b, ρ_i	Bulk density, solid ice density
RICE	Rosemount Icing Detector Probe
SAL	Saharan Air Layer
S_i	Supersaturation with respect to ice
σ	Volume extinction coefficient
Size	Diameter as found from the diameter of a circle fully enclosing a 2D particle image
Small particles	Ice crystals or droplets <50 μm in diameter
t	Time
T, T_{CB}	Temperature, estimated cloud base temperature
TEFLUN-B	TRMM Texas–Florida Underflights
TRMM	NASA Tropical Rain Measuring Mission
V	Particle volume
V_t	Terminal velocity
w	Vertical air velocity
X_l, X_i, X_v	Mixing ratios of liquid, ice, vapor
X_{CB}, X_T	Mixing ratio of cloud base vapor, vapor + liquid + ice

aerosol spectrometer (CAS) probes at a rate of 1 Hz. These PSDs were averaged over 5-s periods to coincide with the 2D probe averaging times, except when noted. It is now generally accepted that large particles shatter on the leading surfaces and inlets of the "small-particle" probes, producing fragments that enter the probes' sensing area and are sampled as true small particles (Field et al. 2006). Concentrations measured by the small-particle probes in mixed-phase and ice-only regions are thus a combination of true particles, when such exist, and shattered particles. The shattered particles must be considered if those data are to be used reliably. According to Heymsfield (2007), linear relationships exist between the IWC in small (FSSP or CAS) and large (2D) particles when relatively few small particles are present (e.g., near the bases of snow virga). Linear relationships also hold between the total projected areas (A) in small and large particles. He expressed these relationships representing shattering analytically and obtained coefficients that characterized the magnitude of the shattering effect on IWC or A derived from the small-particle probes. In appendix A, we further show that linear relationships exist between the total concentration of particles measured by the small-particle probes N_s and the IWC_{2D} or A_{2D} from the data for each field program. We account for the shattering contributions to N_s by subtracting an estimate of the contribution from shattering based on the value of IWC_{2D}.

Vertical motions are derived principally from air motion sensing systems (unavailable for ACTIVE). We have removed periods when the wind vane measurement systems were adversely affected by icing or otherwise produced unreliable results. Aircraft sampling airspeeds ranged from 80 to 180 m s^{-1}, depending on the aircraft used, whether the Grob Egrett, the University of North Dakota Citation, or the NASA WB-57F or DC-8.

3. Results

This section presents observations for those periods when appreciable concentrations of small particles, 3–50 μm in maximum dimension, are identified from the FSSP or CAS data for the seven field programs. The steps used to identify these periods and to mitigate the small particle shattering effects are given in appendix A. Briefly, we use the method described by Heymsfield (2007) to identify times with significant numbers of small particles, drops and/or small ice for each field program. We then subtract out an estimate of the contribution of shattering for each value of N_s. When possible, the analysis uses RICE probe data or laser diode hygrometer data to identify periods when supercooled liquid water is present and to validate the methodology.

a. Presence of small particles and supercooled liquid water

Figure 2 shows Geostationary Operational Environmental Satellite (GOES) visible satellite imagery of the intense convective cell sampled during C-F. The convective cell formed along a sea breeze boundary and the anvil drifted toward the southwest. Figure 3 shows the total concentration of small particles observed in the cloud. Concentrations of droplets, reaching hundreds of inverse cubic centimeters, reflect high CCN associated with a continental air mass but African dust was not responsible in this case. One-half of the high concentration points are in updrafts >4 m s^{-1}, and many of those are at −34°C are where the RICE probe detected liquid water and where graupel was observed with 2D and CIP probes.

Two cases from NAMMA were studied in detail. Just prior to penetrations of updraft cores on 12 September 2006 (Tropical Depression 8, pre-Hurricane Helene), imagery from the Lidar Atmospheric Sensing Experiment (LASE) downward- and upward-viewing UV differential absorption lidar (DIAL) showed a layer of high aerosol extinction (proportional to the scattering extinction ratio)—that is, dust—extending from the ocean surface to about 4 km (all heights MSL; Fig. 4). A dropsonde released at 1240 UTC (time indicated in Fig. 4) when the DC8 was about 110 km west of the updraft core support the LASE humidity observations. A moist layer was located from the surface to 1.7 km, coinciding with a thin cloud layer in the LASE data near 1.0 and 1.7 km. The SAL, as determined from the LASE aerosol scattering signal, was located from about 1.7 to 3.2 km; the LASE shows the top of the layer to be at about 3.0 km at this time. We conclude that the SAL and the boundary layer below it contained appreciable dust.

Concentrations of 3–50-μm diameter particles[1] in the NAMMA observations are large (Fig. 5). The 3–50-μm particles observed near −20°C (20 August), where the relative humidity exceeds 97%, are likely to be droplets, whereas those at −44°C (12 September) are likely homogeneously nucleated ice particles. The highest concentrations observed at −44°C correlate well with the observations of high aerosol loading in the boundary layer and occur in the strongest updrafts (see also Fig. A1). The CVI probe supports this conjecture: a high proportion of the residuals of the sublimated ice particles

[1] The contribution to the high observed concentrations if dust were present is insignificant. Out of cloud and for temperatures above 10°C on 12 September where dust might have been sampled by the CAS probe, the mean concentration of aerosols 2 μm and above was only 3.5 cm^{-3}; 90% of the time the concentrations were below 12 cm^{-3}, and scavenging and parcel expansion would have further reduced the concentrations.

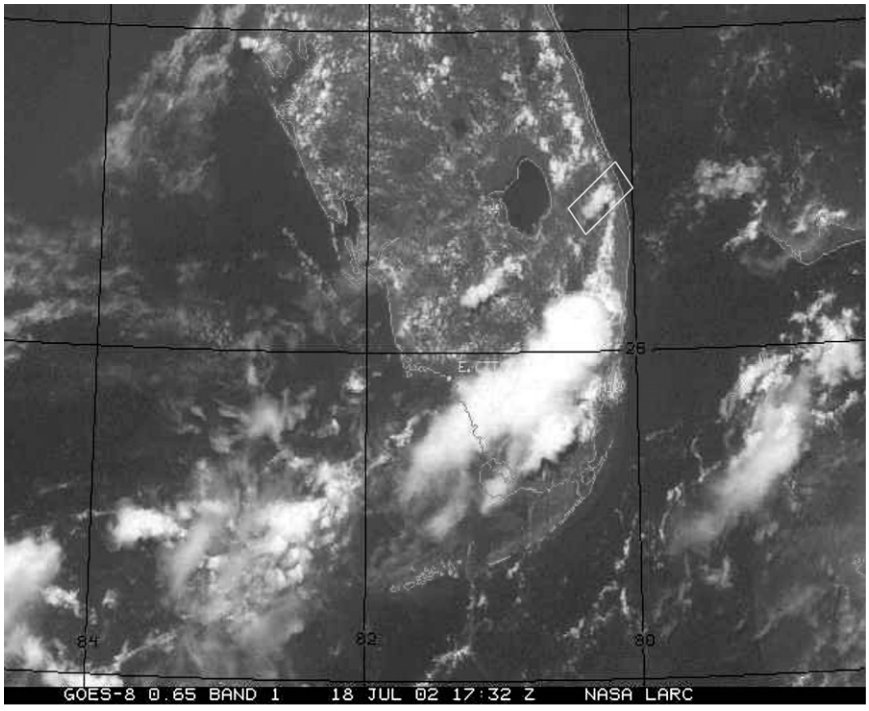

FIG. 2. GOES satellite image of the convective cloud sampled on 18 July 2002 during C-F (rectangular box), taken at 1732 UTC, about 14 min prior to the aircraft penetration. (After Heymsfield et al. 2005.)

were composed of dust (A. Heymsfield and C. Twohy 2009, unpublished manuscript). Small graupel is observed at −44°C. Note that heterogeneously nucleated ice would likely contribute 1 cm^{-3} or less at temperatures above −38°C, even when dust conditions are involved (DeMott et al. 2003), and thus would not be plotted with the scale used.

We compared the concentrations of small particles aloft with those measured just above cloud bases in the SAL for the 12 September case (not plotted). With cloud-base updraft velocities reaching 2 m s^{-1}, droplet concentrations reached more than 1000 cm^{-3}. The clouds we sampled obviously had strong features of continental convection.

During CAMEX-4, the NASA DC-8 penetrated updrafts in the eyewall and in rainbands associated with Hurricane Humberto (Fig. 6). Concentrations of small particles of up to tens of inverse cubic centimeters (see Figs. 7 and A4) are much larger than those expected for heterogeneous ice nucleation and correlate well with updraft strength, especially on 23 September, suggesting that nucleation was by homogeneous freezing of droplets. A comparison of the pristine environment associated with Humberto with that sampled on 12 September during NAMMA, both with strong updrafts, argues for an important role of dust aerosols on the homogeneous nucleation process and more generally on microphysical processes operating in the updrafts.

With RICE probe data available from the three TRMM field campaigns, we are able to correlate the presence of supercooled water with temperature and to evaluate the reliability of our estimates of N_s when cloud droplets are prevalent. The RICE and FSSP probes are designed to collect data at a rate of 1 Hz, and we take advantage of that temporal resolution here. The RICE probe worked throughout all three field campaigns, leading to 78 000 1-s points. Icing of the pitot tubes resulted in considerable loss of vertical wind data, and FSSP failure during KWAJEX further reduced the amount of useful data. Even so, 40 000 in-cloud points where the FSSP registered particles were collected at temperatures below −5°C and 11 000 points were collected at temperatures below −20°C.

In the TRMM LBA dataset at temperatures near −40°C, we find occurrences of 10–100 cm^{-3} of small particles (Fig. 8). The largest concentrations are located primarily in updrafts >5 m s^{-1}, and with temperatures approaching the threshold for homogeneous nucleation (Fig. 8c) they are likely ice. Few >5 m s^{-1} updrafts were sampled below −20°C from KWAJEX (Fig. 9). Liquid water is found frequently at temperatures from 0° to −10°C but diminishes below that temperature range

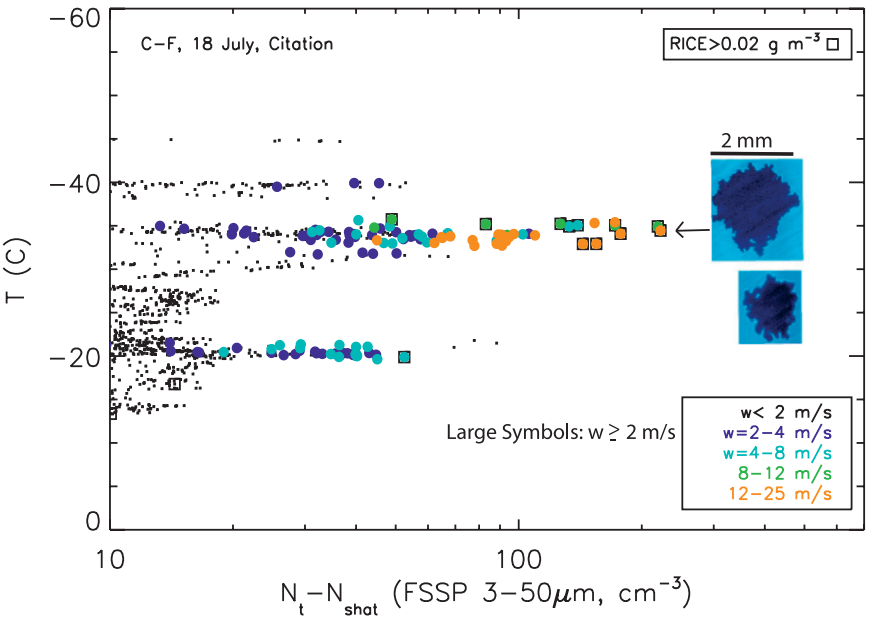

FIG. 3. Particle concentration (3–50-μm diameter), with estimated shattering removed (cf. Fig. A2), as a function of temperature, for C-F, 18 Jul 2002. Points where liquid water was detected from a RICE probe are shown. Vertical air velocities (w) are color coded, with the bins shown in the lower right (m s^{-1}). The large symbols are where $w \geq 2$ m s^{-1}; boxed symbols indicate where there is detectable liquid water as measured by a Rosemount Icing probe.

(Figs. 8b and 9b), primarily in updrafts (Figs. 8d and 9d). Apparent trends of decreasing concentrations of small particles with decreasing temperatures are noted (Figs. 8c,d and 9c,d), a feature likely to indicate droplet removal through accretion. Not shown here are the few observations of small particles, which are likely drops given the >-30°C temperatures observed for TRMM TEFLUN-B.

Figure 10 shows the distribution of RICE-derived LWC with temperature for the three TRMM field programs. Occurrences of liquid water are reliable where the RICE LWC exceeds about 0.02 g m^{-3}. All points are shown, with those where the vertical velocities exceeded 2 m s^{-1} dominating the LW regions. Liquid water largely disappears in the updrafts for temperatures below -20°C, consistent with the results of Stith et al. (2004) based on several case studies during the TRMM field campaigns. Note that the clustering of points at specific temperatures is related to the sampling strategy.

The sampling aircraft used for ACTIVE, an Egrett, is relatively fragile, so strong updrafts and neighboring regions were deliberately avoided. Only one of the four Hector storms exhibited a signature of small particles and homogeneous nucleation for a few 5-s periods. Unambiguous high concentrations of small ice particles, about 125 cm^{-3}, were observed at temperatures near $-42°$ and -52°C in one of the two squall line cases. None of the three monsoon clouds indicated a signature of homogeneous ice nucleation. Because there are relatively few periods of homogeneous nucleation sampled during ACTIVE, they are not plotted here. (More details are shown in Figs. A5 and A6.)

One of the nine C-F cases sampled by the WB57-F suggests an enhanced concentration of small particles, presumably homogeneously nucleated given the <-50°C temperatures. Concentrations reached 20 cm^{-3} for about a dozen periods. (These are not plotted here but are shown in Figs. A5 and A6.)

b. *Synthesis of data*

Stith et al. (2004) reported on the results of a composite microphysical dataset that represented all the available 1-Hz data in and near updraft regions from LBA and KWAJEX. They examined the temperature dependence of the vertical velocities and liquid water contents as measured by a King probe, a less sensitive indicator of the LWC than the RICE probe. Aerosol conditions were characterized as being clean. Anderson et al. (2005) reported on in situ measurements of updrafts at 1 Hz from TRMM LBA and KWAJEX and compared them to previous studies of tropical updrafts. The median values of the average updraft velocity for the cores for both projects increased from about 2 m s^{-1} near cloud base to 3 m s^{-1} in the 6–7-km altitude range. The highest values of the updraft speed, expressed as the upper 10% of the updraft velocities, increased with height, from about 4–6 m s^{-1} at 1.5 km to 8–10 m s^{-1} at

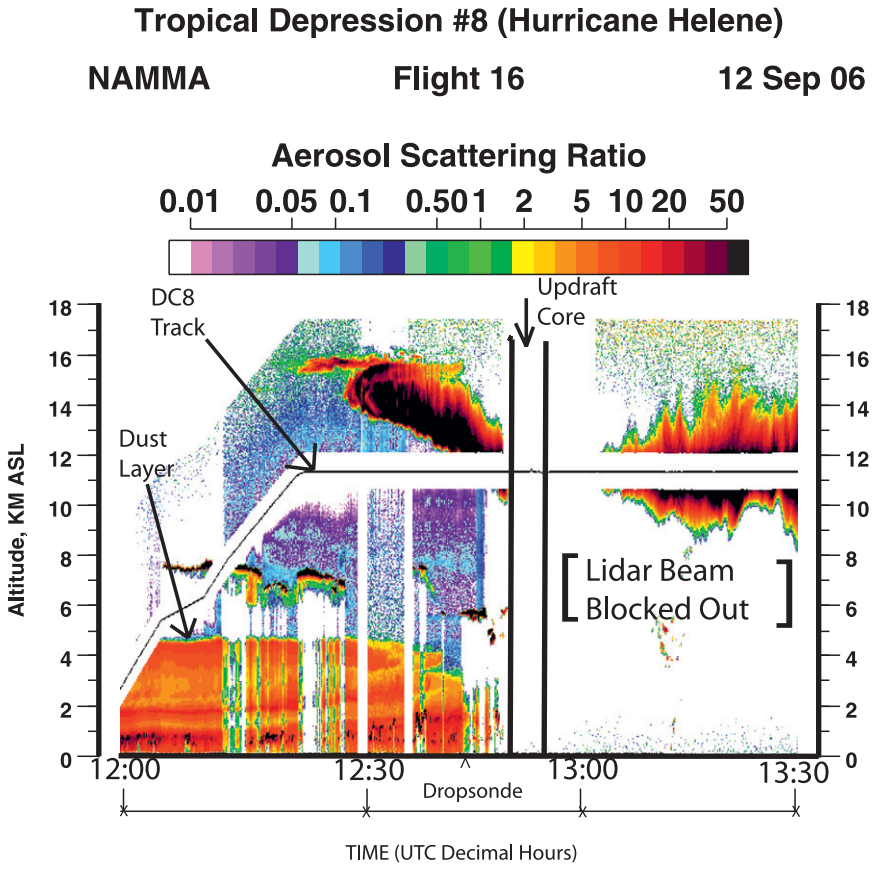

FIG. 4. Lidar imagery from LASE DIAL looking upward and downward from the NASA DC-8 on 12 Sep 2006 during NAMMA. The DC-8 altitudes are indicated by the nearly horizontal solid line. The dust layer appears from 1200 to 1245 UTC at 5 km and below. The updraft encounter was from 1252 to 1253 UTC, shown between the dark vertical lines. The time of release of a dropsonde from the DC-8 is shown. The lidar beam was blocked by cloud for those periods when the ocean surface is not detected in the figure.

6 km. The observations were consistent with earlier studies of low-latitude (20°N to 20°S) maritime convection (Zipser et al. 1981). Sampling in our study was primarily from updrafts at heights of 7 km and above, where the earlier studies left off. To reach these levels, updrafts in the cases we investigate are likely to be stronger, on average, than for the earlier studies.

In this section, we broaden the Stith et al. (2004) analysis for a wider range of conditions. We select the data from the seven field programs reported on in section 3 for those periods when there were relatively large concentrations of small particles. Our goal is to quantify when supercooled drops can survive uncaptured or unfrozen to homogeneous nucleation temperatures in primarily low-latitude maritime convection or continentally perturbed maritime convection at latitudes from 25°N to 10°S. Our sampling strategy did not allow for following the temporal evolution of particles in individual updrafts relative to the time of the updrafts' initiation or for measuring vertical profiles of the microphysical, thermodynamic, and dynamic structures in individual updrafts. We can therefore look only for trends that may be of a general nature and use those results as input into a parcel model to study further the fate of droplets in updrafts (section 4).

We selected periods with the high likelihood of the presence of small particles and then adjusted the concentrations of small particles downward to account for shattering (appendix A). There were 1091 5-s such encounters[2] at temperatures of −20°C and below for all field programs. Of this dataset, 75% of the encounters are at temperatures −38°C and below. Encounters were reasonably well distributed according to the field program

[2] Averaging over 5-sec intervals was necessary to reach a good statistical sample of data from the particle probes. This process would have smoothed out the peak updraft velocities.

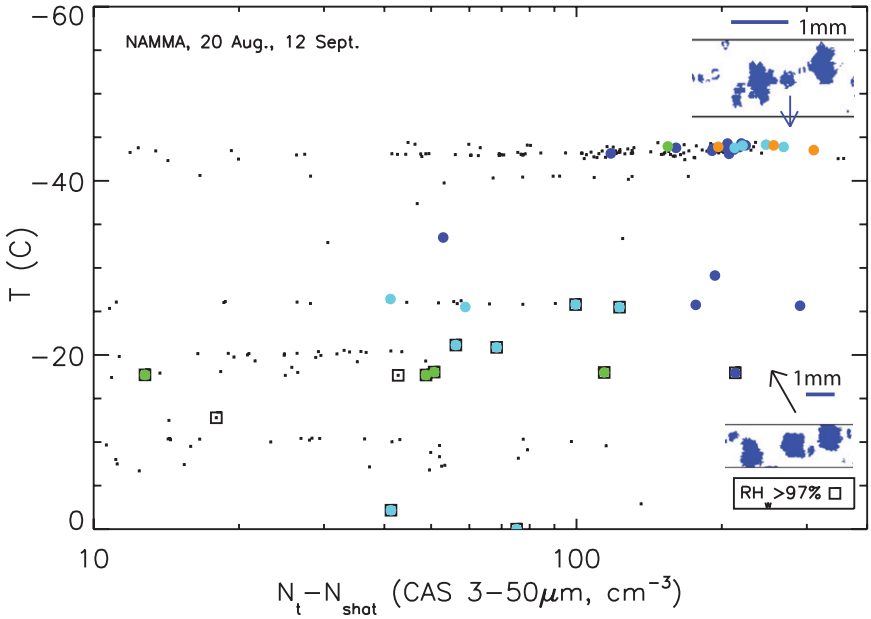

FIG. 5. As in Fig. 3, but for NAMMA cases on 20 Aug and 12 Sep 2006. Regions with relative humidities near water saturation (RH > 97%), vertical velocities, are highlighted.

except for ACTIVE (Table 2a). However, there was unavoidable selection by temperatures largely for safety and programmatic reasons (Table 2a). For all field programs except TRMM, the temperatures in the mean were close to or below the temperature required for homogeneous nucleation; for TRMM, droplets were not observed in the updrafts at temperatures below about −20°C.

Of our sample, 42% of the vertical velocities (w) are in downdrafts and 58% in updrafts, distributed as shown in Table 2b. Updrafts above 10 m s^{-1} were noted for all the field programs, with no dependence of temperature noted (Fig. 11a). The median downdraft and updraft speeds of the sample of points are −1 and 2 m s^{-1}, respectively. The 1-Hz values of the updrafts would have shown higher peaks and lower minima, but the averaging for 5 s was necessary for obtaining reliable PSD from the large-particle probes. The data for ACTIVE are not included in these vertical velocity statistics because vertical velocity was not measured.

Total concentrations of small particles, with diameters from 3–50 μm, peaked in the 25–100 cm^{-3} range (Table 2c). The highest frequency of occurrence was noted in this range rather than in the 1–10 or 10–25 cm^{-3} ranges because the stringent criteria we used for identifying true encounters with high concentrations of small particles selectively identified high concentration events. Concentrations exceed 100 cm^{-3} for C-F and NAMMA (Fig. 11b) where landmass may have enhanced CCN feeding into the updrafts. Where temperatures are >−38°C these are likely mostly droplets and below these temperatures are likely homogeneously nucleated ice.

The median value of the condensed water content (CWC) in small particles is 0.12 g m^{-3} and the peak value is 0.9 g m^{-3} (Fig. 11c). The median increases from about 0.09 to 0.14 g m^{-3} from −20° to −60°C. (All small particles are taken to be solid ice spheres. Where liquid water dominates, at temperatures above −38°C, these values could be up to 10% larger because of the difference in solid and liquid water densities.) The observed CWC increase with altitude is notable because the expansion of a parcel between the −20° and −60°C levels should lead to a 40% decrease in the CWC. The observed increase is due primarily to a net increase in the number concentration of small particles upward. Some of the observed increase may be circumstantial because different field programs contribute to different temperature ranges in the figure. Nonetheless, we suggest that the increase in the CWC in small particles is primarily the result of additional droplet activation in the updrafts, a point further examined in section 4.

The IWCs (in units of grams per cubic meter) in large particles were derived from the PSDs and assumptions about particle masses and densities (appendix B). While the CVI provides the most direct measurement of CWC, it was often saturated in the high-CWC regions associated with strong updrafts examined here, so it was not used for the bulk of the analysis. Favorable agreement between the IWC_{2D} and CVI CWC is found when the two could be compared (appendix B). The IWC_{2D} values

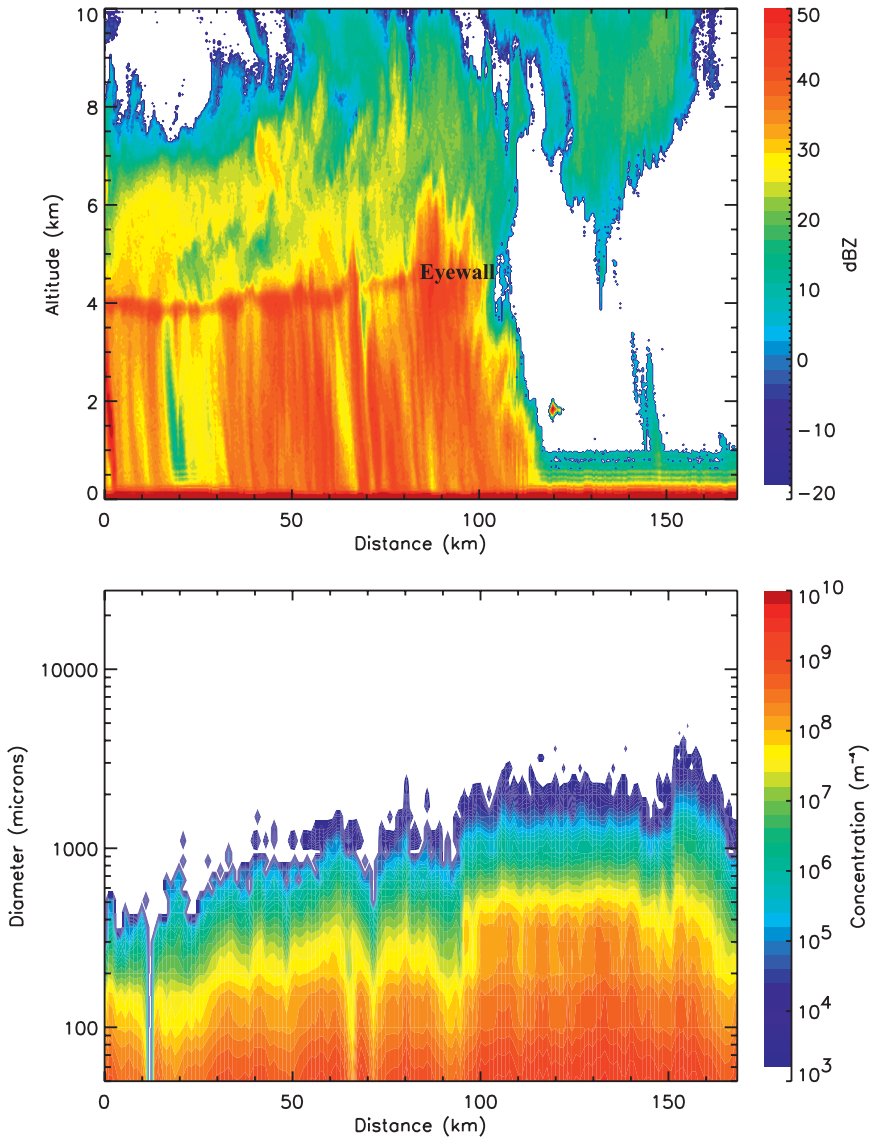

FIG. 6. Radar imagery from the Jet Propulsion Lab (JPL) Precipitation Radar 2 (PR2) radar on 25 Sep 2001 from 0019:39 to 0032:29 UTC. The location of the eyewall is shown. (After Heymsfield et al. 2005.)

decrease on average by a factor of 3 from −20° to −60°C, with a median IWC_{2D} of 0.54 g m^{-3} and a peak value of 2.8 g m^{-3} (Fig. 11d). The highest values are noted for the TRMM and CAMEX campaigns, lower for NAMMA, and lowest for ACTIVE and C-F. Differences may be related to maritime versus continental CCN concentrations. If we increase particle masses by 50% to cover the upper limit expected for the particles (appendix B), the median IWC_{2D} increases to 0.75 g m^{-3} (see curve in Fig. 11d). Gravitational settling and fallout of the large ice and entrainment must account for most of the observed factor of 4 decrease with temperature because the air density would lead to a net decrease of only 40%.

Figures 11e and 11f show the total projected area A in small (≤50 μm; A_s) and large (>50 μm; A_{2D}) particles. The former are derived assuming that the small particles are spherical, and the latter are derived from the 2D particle images. Notable increases in A_s (e.g., at −43°C) and decreases in A_{2D} are found with decreasing temperature (e.g., at −53°C). Furthermore, values of A_s are considerably larger than those of A_{2D} at the lower temperatures, pointing out the radiative significance of the small particles.

The radiative impact of the small particles can be characterized from the effective diameter D_{eff} given by

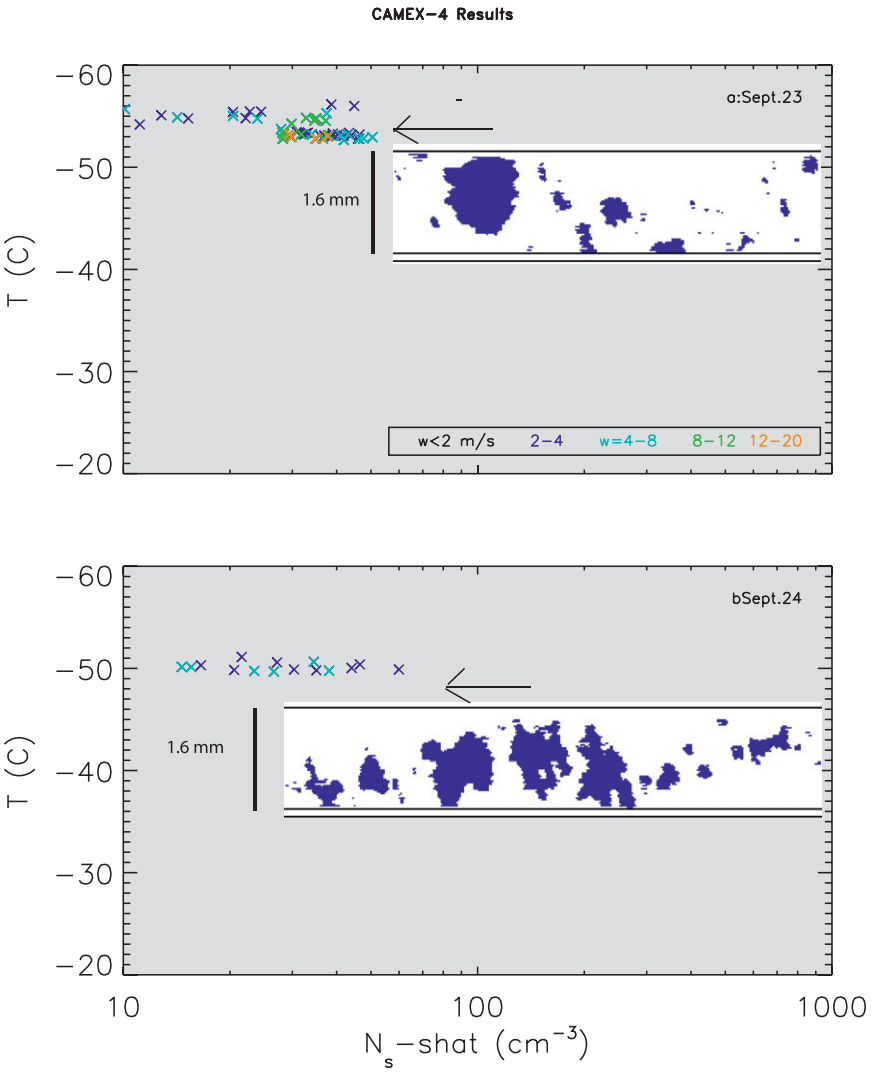

FIG. 7. Particle concentration (3–50-μm diameter), with estimated shattering removed, as a function of vertical velocity for Hurricane Humberto sampled on 24 Sep 2001 during CAMEX-4. Vertical velocities are color coded.

$$D_{\text{eff}} = \left(\frac{3}{2}\right)\left(\frac{\text{IWC}}{\rho_i A}\right), \tag{1}$$

where IWC and A are the sum of the values in small and large particles and ρ_i is the density of solid ice.

We use the results shown in Figs. 11c–f to derive effective diameters in the small particle regions. Because the regions we have identified as containing small particles include the source regions—updrafts, debris regions, downdrafts, and differing aerosol source regions—a wide range of effective diameters is observed (Fig. 12). Small values of the effective diameters, about 20 μm, are observed in the regions of high concentrations of small particles, primarily from NAMMA and to a lesser extent C-F. Effects of continental aerosol populations and especially dust on the effective diameters as a consequence of homogeneous ice nucleation contribute to highly reflective convection.

The amount of large ice reaching the −20°C level is key in understanding subsequent droplet depletion in the updrafts. The large ice depletes cloud droplets directly by accretion and indirectly by vapor diffusion onto the ice. The total water mixing ratio X_T in a volume of air, normalized by the amount of water vapor flowing into cloud base X_{CB} is given by

$$\frac{X_T}{X_{\text{CB}}} = \frac{(X_v + X_s + X_{\text{2D}})}{X_{\text{CB}}} \tag{2}$$

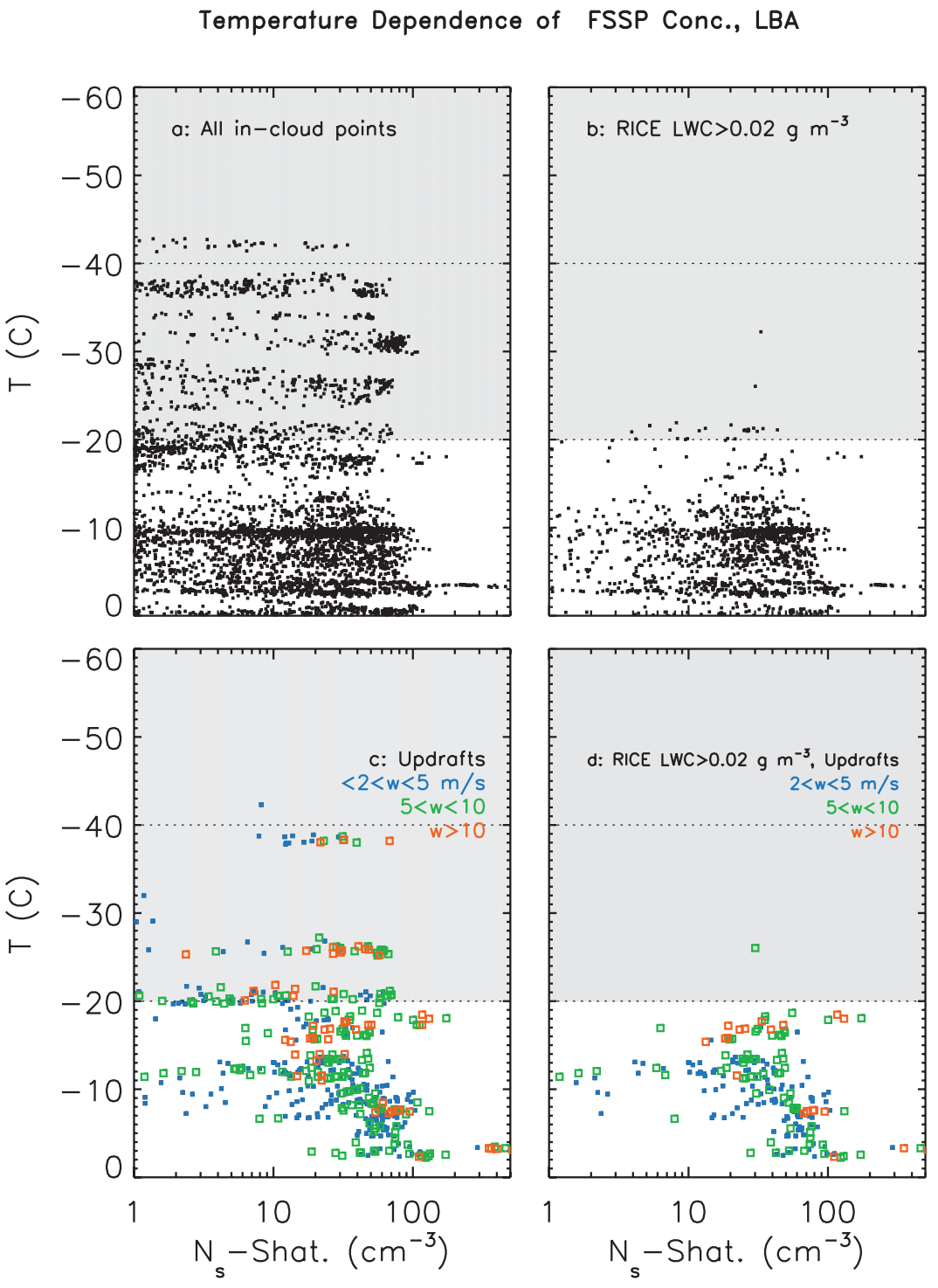

FIG. 8. Particle concentration (3–50-μm diameter) for the TRMM LBA dataset, with estimated shattering removed, showing (a) all in-cloud points, (b) only points where the estimated LWC from the RICE probe >0.02 g m^{-3}, (c) only points where the vertical velocities are >2 m s^{-1}, and (d) points where RICE LWC >0.02 g m^{-3} and updrafts >2 m s^{-1}. In (c) and (d), the points are color coded according to the vertical velocity range in m s^{-1}.

and provides a relative measure of precipitation efficiency and indirectly a way to characterize the ability of small particles to be lofted to homogeneous nucleation temperatures. The mixing ratio of vapor X_v is derived by assuming that the air is saturated with respect to water at the measurement temperature.[3] The mixing ratios of liquid or frozen small particles X_s and large ice X_{2D} are taken to be IWC_s and IWC_{2D}, normalized by the local air density. Cloud base temperatures (T_{CB} and X_{CB}) have been estimated from observations taken from a combination of aircraft soundings, dropsondes launched from aircraft, and ground-based soundings taken in close proximity and time to the aircraft in situ measurements for most of the cases studied here.[4]

The subset of X_T/X_{CB} estimates in updrafts exceeding 2 m s^{-1}, connected directly to cloud base and where there are relatively few contributions from ice particles falling into the measurement level (see discussion below), are shown in Fig. 13. This partitioning attempts to connect the observations more directly to the updrafts and to reduce the effects of sedimentation of ice particles from above. The median value of the fraction for all cases is 0.13 (Fig. 13, lower right). Beginning with a fraction of 0.23 (23%) at −20°C, X_T/X_{CB} decreases linearly by about 1.5% per 5°C (see solid curve). We surmise that there is considerable fallout of condensate in large particles through the updrafts before a parcel reaches −20°C and that this trend continues through the temperature range −20° to −60°C (e.g., Fig. 11d). In the mean, there is little dependence of the ratio of X_T/X_{CB} on the vertical velocity. In appendix B, we look further at how the ratio of X_T/X_{CB} depends on the assumptions we made about ice particle densities.

To look further into whether precipitation processes can account for the changes in the ice mass mixing ratio between −20° and −60°C, we have examined the changes in the slopes λ and intercepts N_0 of exponential PSD fitted to the measured PSDs, and in the maximum diameter of the particles over this temperature range (Figs. 14a–c). For the group as a whole, the mean value of $\lambda = 45$ cm^{-1}, with little dependence on temperature. Broad spectra (values of λ of $<$ about 20 cm^{-1}) were sampled for C-F and CAMEX-4 and relatively narrow spectra for TRMM (Fig. 14a). The value of N_0 decreased with temperature, with a median value of 6.6 cm^{-4} and a mean value of 19 ± 40 cm^{-4} (Fig. 14b). The decrease in IWC_{2D} with height is largely related to the decrease in N_0 because the two are proportional for a given value of λ. There is a steady decrease in D_{max} upward, from a mean of about 0.5 cm near −20°C to 0.2 cm near −60°C (Fig. 14c). This trend suggests that the large ice particles are settling through and out of the updrafts, accounting in part for the decrease in IWC_{2D} upward.

The rate of collection of droplets by a population of large ice is proportional to their differential fall velocity (appendix C). We have calculated mean mass-weighted fall speeds for the PSD at the measurement (pressure) level based on the nondimensional, Best number/Reynolds number approach of Mitchell and Heymsfield (2005). Four scenarios are examined: using the mass–dimensional relationship based on the C-F observations for anvil and thick ice cloud (Heymsfield et al. 2004), 1.5 times those masses, and a density assumed for all particles of 0.2 and 0.3 g cm^{-3}, respectively. Because the large particles are nearly spherical, they are assumed to have circular cross-sectional areas. On average, the different scenarios produce mass-weighted mean fall speeds of 150 to 200 cm s^{-1} throughout the temperature range of interest (Figs. 14d,e).

The rate of sweepout of cloud droplets by large ice is proportional to the cross-sectional area of the large particles A_{2D}. Since this parameter decreases upward in the updrafts (Fig. 11f), we wondered whether the decrease was associated directly with the fallout of large ice. Given the nearly monotonic relationship between IWC_{2D} and A_{2D} (Fig. 14f), it would appear that the rate of sweepout of droplets in the updrafts by large ice decreases in response to the fallout of large ice. Thus, the probability of sweepout of droplets by large ice diminishes with altitude in the updrafts.

4. Discussion

This section further investigates the presence and significance of droplets lofted by the updrafts to temperatures required for homogeneous ice nucleation. Using the results from section 3 as input into a parcel model, we calculate the updraft velocities required for

[3] The saturation mixing ratio at −20°C is about 2 g kg or about 10% of the cloud base value. A reasonable 10% error in the assume RH produces a potential error in Eq. (2) of only 1%.

[4] TCB values were 23.5°C ± 0.25 for the intense updraft sampled during C-F as derived from two nearby (Miami) soundings at overlapping times, 23.5°C for the 20 August NAMMA case from DC8 sampling just above cloud bases, and 23.5°C for the 12 September NAMMA case from two dropsondes that descended through the dust layers. For the CAMEX-4 cases, TCB are taken to be 22°C (R. Black 2008, personal communication). Soundings launched near the times of sampling for the 22 January ACTIVE squall line case, KWAJEX, and LBA cases gave approximate TCB values as 24 and 22°C. Uncertainty in TCB produces a 6% uncertainty in XCB when TCB = 22°C for a cloud base pressure of 900 hPa. For all cases, cloud base height is taken to be 933 hPa and 700 m, which is an approximate average for the cases.

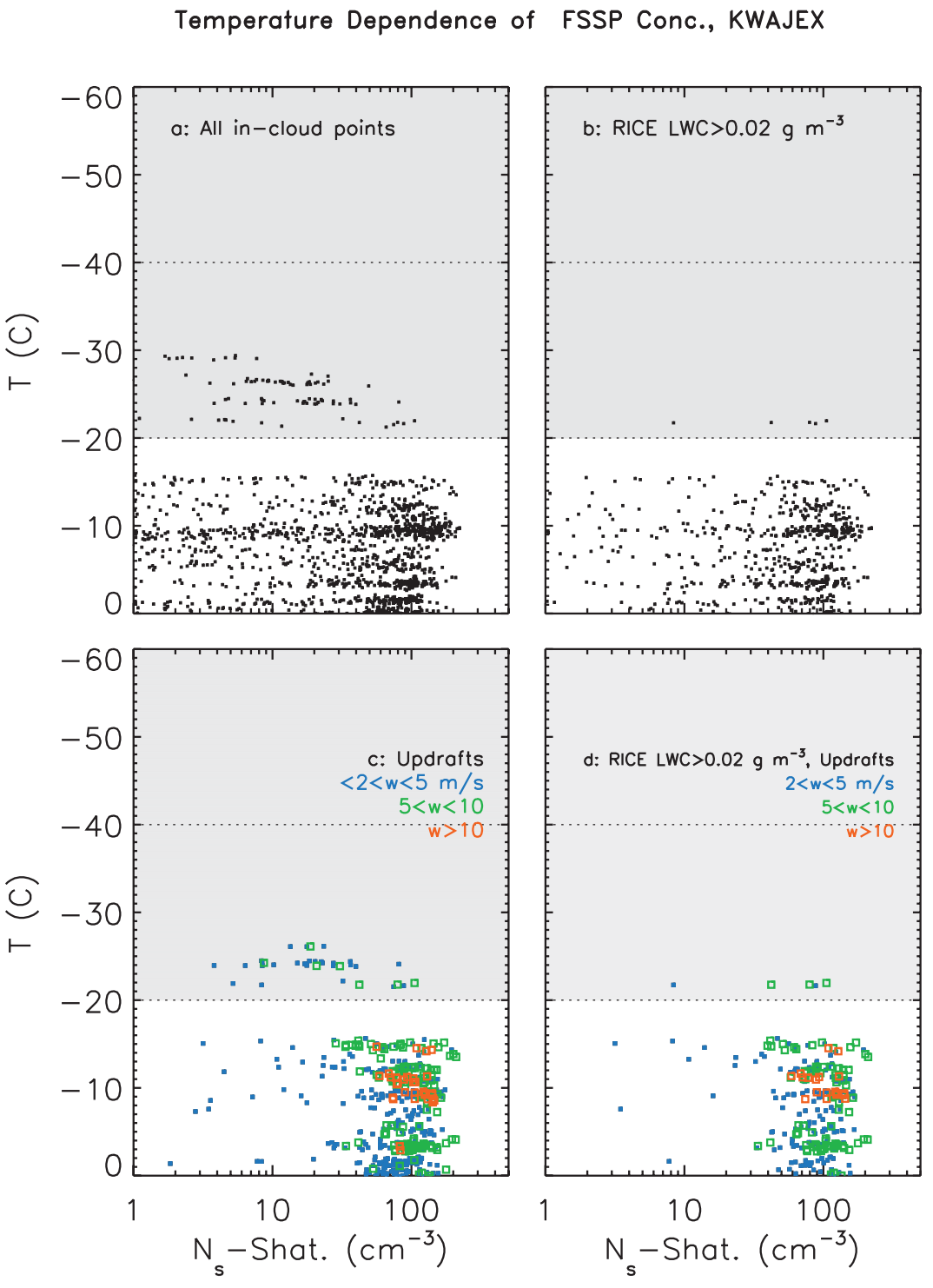

FIG. 9. As in Fig. 8, but for TRMM KWAJEX.

a population of droplets with given LWC to be lofted from −20° to −38°C.

A 1D parcel model developed by Heymsfield et al. (2005) quantified the IWC required to permit homogeneous nucleation to occur for the C-F updraft sampled on 18 July (Fig. 3). Droplets were activated and grew in updrafts of up to 20 m s^{-1}. Large ice (100 μm–3 mm) was introduced into the updrafts in concentrations given

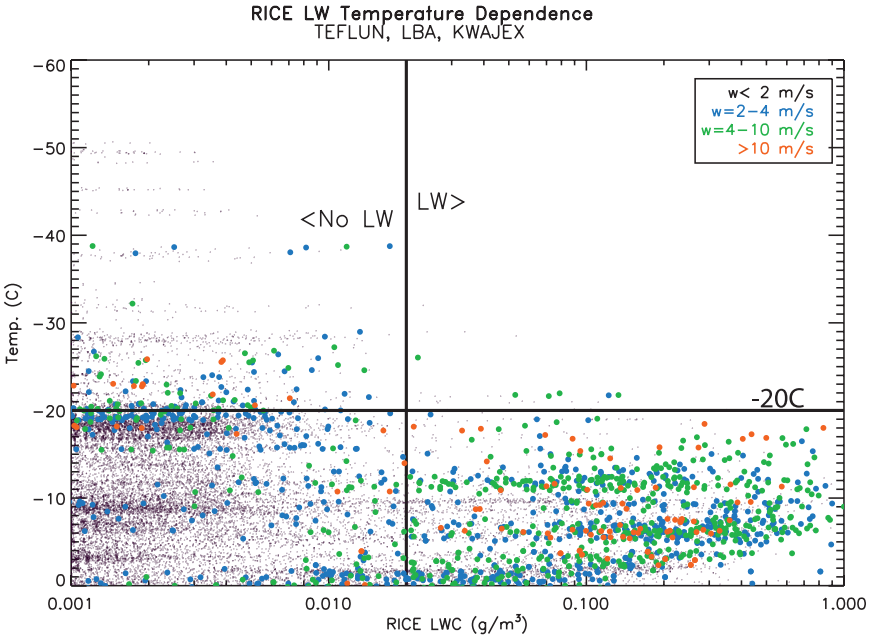

FIG. 10. Summary of LWC estimated from the RICE probe from the TRMM field programs TEFLUN-B, LBA, and KWAJEX. Data are at 1 Hz. The vertical line at 0.02 g m^{-3} marks the approximate division between data (right) and noise (left). Vertical velocities are color coded where updrafts >2 m s^{-1}.

by a gamma distribution with slope $\lambda = 20$ cm^{-1} to approximate the relatively broad distributions found in the updrafts, dispersion parameter parameterized as a function of λ, and intercept N_0 derived from the IWC specified for the large ice. The total water content was conserved. The large ice depleted vapor and droplets via diffusional growth. Accretional growth of the large ice was not considered. The fraction of the droplets that could be lofted to −38°C increased from near zero for updrafts of 4 m s^{-1} to near unity with 7 m s^{-1}.

Two 1D parcel models were developed here (appendix C) to better quantify the growth of the large ice and the depletion of the droplets in updrafts. The model physics considers droplet collection by accretion, growth of the large ice by diffusion and accretion, and droplet growth via condensation, offset by vapor liberation due to parcel cooling. Model 1 conserves total water, thereby neglecting both 1) the net transfer of ice mass resulting from fallout into and out of parcels and 2) entrainment. Model runs indicate that both the IWC in large particles and the maximum particle size increase upward. These trends run counter to those observed (see Figs. 11d and 13c) because the particles are not allowed to fall out of the updrafts, and this model was abandoned.

Model 2 uses the observations in Figs. 11–14 as model constraints. The observed mean relationship $IWC_{2D} = 2.74e^{0.036T(°C)}$ from Fig. 11d is used to specify the vertical profile of the IWC in large particles. The appropriate amount of IWC is removed from the parcel as it cools, allowing the ice particles to take up droplets and vapor, but also for the ice mass to fall out of the parcel. In each 1-s model time step,

- The vapor made available due to parcel cooling is first taken up by diffusional growth of the large ice. These particles grow with a density of 0.91 g cm^{-3}.

TABLE 2. Summary of observations.

Distribution of Cases by Field Program		
NAMMA	15% of total	$\overline{T} = -39.2 \pm 7.4$°C
CRYSTAL-FACE	16%	$\overline{T} = -34.2 \pm 5.4$°C
CAMEX-4	56%	$\overline{T} = -52.5 \pm 3.6$°C
TRMM	13%	$\overline{T} = -26.5 \pm 5.9$°C
ACTIVE	<1%	$\overline{T} = -52.1 \pm 1$°C
Vertical velocities		
$w < 2$ m s^{-1}	11% of total	
$-2 \le w < 0$ m s^{-1}	31%	
$0 \le w < 2$ m s^{-1}	31%	
$2 \le w < 4$ m s^{-1}	12%	
$4 \le w < 8$ m s^{-1}	8%	
$8 \le w < 12$ m s^{-1}	4%	
$w \ge 12$ m s^{-1}	3%	
Small particle concentrations		
1 − 10 cm^{-3}	13% of total	
10 − 25 cm^{-3}	25%	
25 − 100 cm^{-3}	52%	
>100 cm^{-3}	10%	

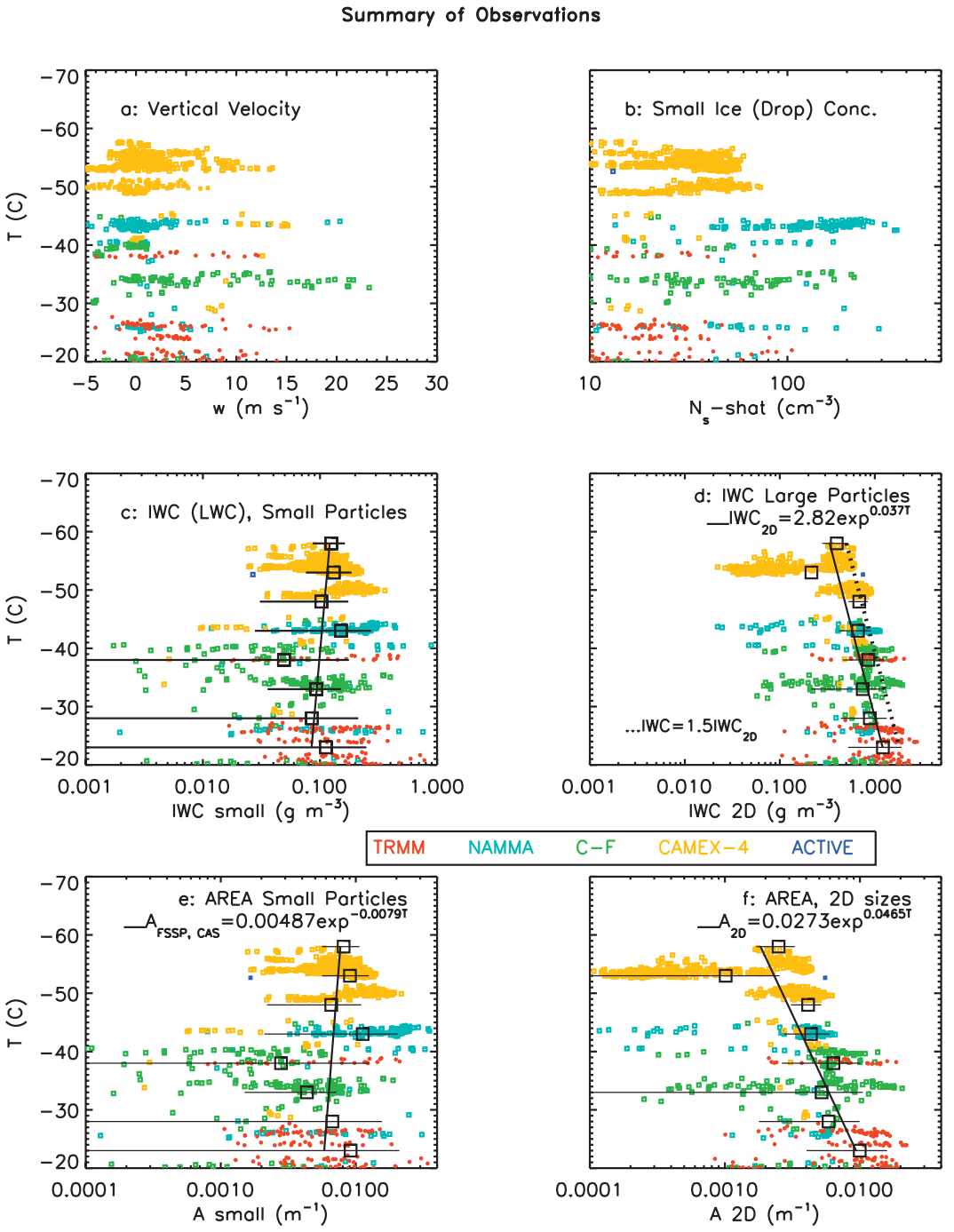

FIG. 11. Data from all identified encounters with small particles as a function of temperature. Where appropriate, median values (squares), standard deviations (horizontal lines), and curve fits (sloping lines) are shown. (a) Vertical velocity. (b) Concentration of small particles, corrected for estimated shattering. Ice water content in (c) small and (d) large particles, with (d) derived using mass–dimensional relationship from C-F (Heymsfield et al. 2004) and also derived from masses that are 50% larger. (e),(f) Total cross-sectional area in (e) small and (f) large particles.

- With water supersaturations, droplets grow; with subsaturations, they evaporate.
- Any residual vapor—above the amount depositionally and condensationally added to the large ice and droplets—is accumulated in the parcel as supersaturation. Any deficit is first subtracted from the supersaturation and then evaporated from droplets.

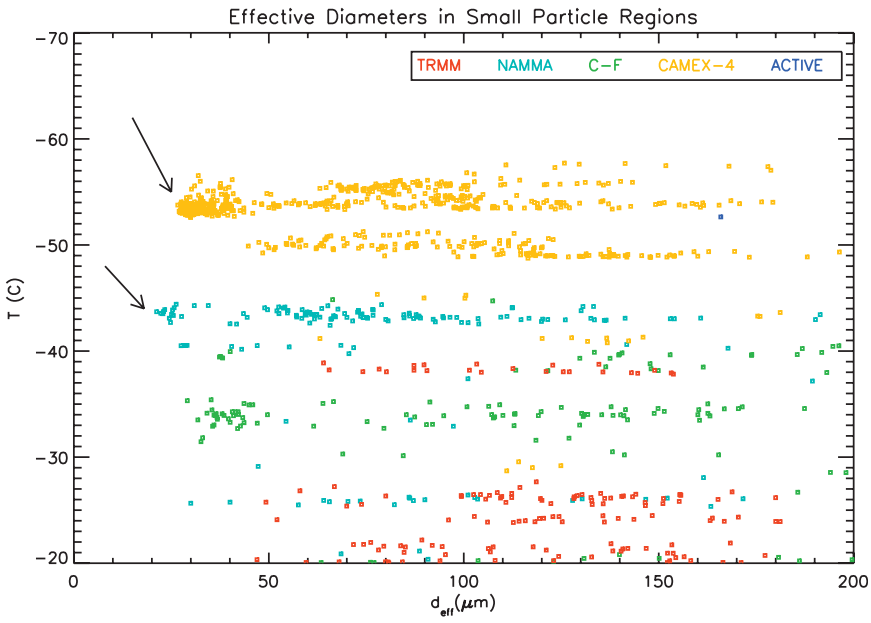

FIG. 12. As in Fig. 11, but for effective diameter as calculated from Eq. (1). Arrows show regions of low values of D_e.

- The large ice collects droplets, with diameter increasing by assuming an ice effective density of 0.2 g cm^{-3}. The accreted droplets are removed from the droplet population.

Initially, parcels are at water saturation with a temperature of −20°C, LWC = 0.1 g m^{-3} (Fig. 11c), and IWC = 1.32 g m^{-3} (Fig. 11d). The droplet spectrum is taken to be monodisperse, consisting of 10-μm-diameter droplets with a concentration given by the LWC. Initially, the concentration is 192 cm^{-3}. The ice PSDs are taken to be exponentials (rather than gamma PSD because they fit the observations) of the form $N = N_0 e^{\lambda D}$,

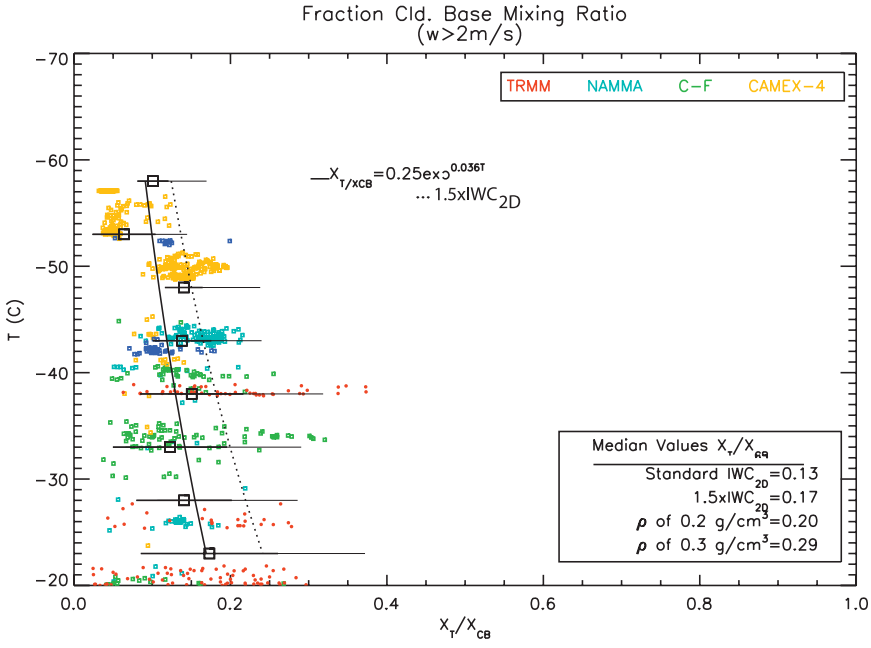

FIG. 13. As in Fig. 11, but for fraction of cloud base air as calculated from Eq. (2) and the associated discussion. The lower right legend shows the median values of the fraction averaged through the layer with different assumed particle masses and densities.

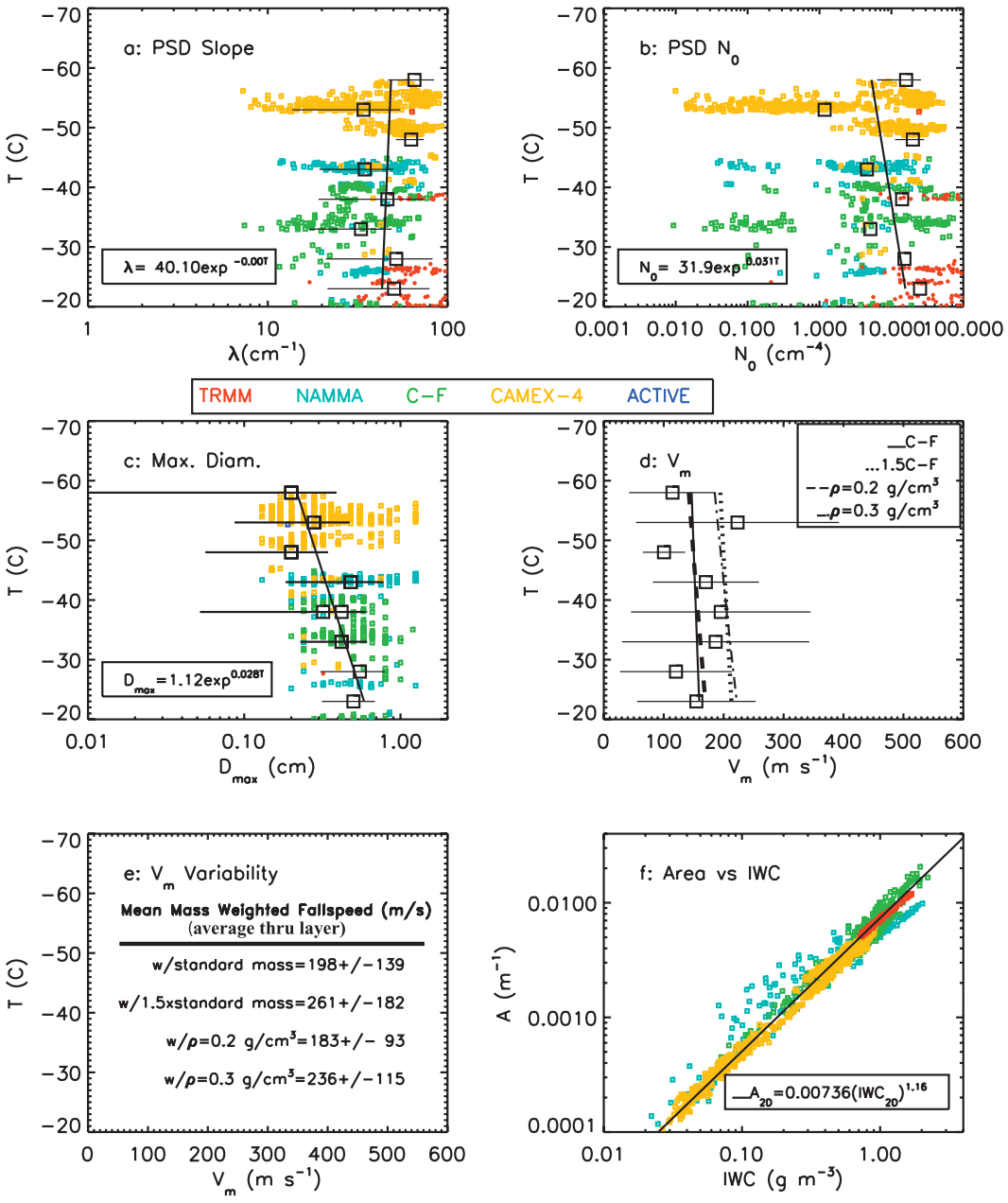

FIG. 14. As in Fig. 11, but for (a) fraction of cloud base vapor reaching the measurement level, for updraft velocities of 2 m s^{-1} and above, (b),(c) slope and intercept parameters of exponential curves fitted to the PSD, (d) maximum diameter for each measured 5-s average PSD, and (e) mean mass-weighted fall speeds estimated from the PSD using different assumed mass–dimensional relationships. These include those developed for C-F, masses that are 50% larger than those, and densities for all particles assumed to be 0.2 and 0.3 g m^{-3}. (f) Relationship of area to IWC for large particles.

with 100 equally spaced diameter bins, from the smallest size at 100-μm diameter to the largest determined by temperature, $D_{\max} = 1.11e^{0.029T}$ (Fig. 14c). With a slope $\lambda = 50$ cm^{-1}, N_0 is given by the IWC. Total concentrations of large ice decrease from about 0.25 cm^{-3} at −20°C to 0.050 cm^{-3} at −40°C.

Some processes in the model are simplified or are not considered. Because of uncertainties in the relationship between the CCN concentrations and the supersaturation and how much of the CCN population is activated near cloud base, we have chosen not to activate new droplets in the updrafts. By ignoring this process, we can

quantify the supersaturation that would build up and learn whether new activation is likely or not. We have also chosen not to include new, additional heterogeneous ice nucleation or ice entrained into the updrafts. Calculations show that these particles would rapidly grow to 100 μm and therefore be included in the IWCs and concentrations of large ice specified by the temperature. Vertical velocities are assumed to remain constant in the vertical. Increasing vertical velocities with height will increase the likelihood for drops to freeze homogeneously. Entrainment is a highly complex process and is therefore not considered directly here. It would reduce the population of droplets and the LWC. Effects of entrainment on the large ice population are treated implicitly by reducing the ice water mixing ratio in large particles upward in the updrafts.

The rates of accretional, diffusional, and condensational growth are compared to the rates of liberation of vapor for three updraft velocities in Fig. 15 (left). With a 4 m s^{-1} updraft (Fig. 15a), the diffusional growth of the large ice exceeds the rate of vapor supply by adiabatic expansion, and the droplets evaporate to supply the needed vapor. Accretional growth further reduces the LWC so that the liquid water is quickly depleted. The diffusional growth rate far exceeds the accretional rate. The relative humidity rapidly falls below 100%. The LWC rapidly diminishes to 0 g m^{-3} (Fig. 15b). With an updraft velocity of 6 m s^{-1} (Fig. 15c), the diffusional rate slightly exceeds the vapor supply rate and, because the relative humidity falls slightly below water saturation, the droplets slowly evaporate. A point is reached (marked with an ''x'' in Fig. 15c) where fallout of the large ice allows the rate of vapor supplied to more than offset the rate of ice diffusional growth and the relative humidity increases again. Liquid water remains to about the −30°C level. For 10 m s^{-1}, the vapor supply rate far exceeds the diffusional growth rate (Fig. 15e), and liquid water content increases until the −40°C level is reached.

Although the LWC can increase to 0.3 g m^{-3} for updrafts of 10 m s^{-1} and increase even more with stronger updrafts, they contribute relatively little to the total water mixing ratio such that the fraction of the cloud-base vapor exhibits the same trend with temperature as observed (cf. X_T/X_{CB}, right side of Fig. 15, and Fig. 13). For the 10 m s^{-1} case, the increase in the LWC with decreasing temperature is similar to the observed IWC or LWC in small particles (Fig. 11c).

The maintenance of droplets in the updrafts is sensitive to the IWC in large particles. To test this hypothesis, we increased the IWC by 50% and evaluated under what conditions drops could be lofted to the −40°C level. For updrafts of 9 m s^{-1} and less, diffusional growth of the large ice overwhelmed the rate of condensate production, and drops were unable to survive the transport. Updraft velocities greater than 9 m s^{-1} were required for homogeneous nucleation.

We can assess whether new droplet activation is possible in the updrafts without undue speculation about the nature of the CCN at cloud base and the supersaturations achieved because the model was designed to allow the excess water vapor to build up rather than to allow it to activate new cloud droplets. In the model, peak supersaturations reached 0.5%, 0.8%, and 1.8% for updraft velocities of 8, 10, and 12 m s^{-1}, respectively. Doubling the IWC through the vertical column and with vertical velocities of 10, 12, and 20 m s^{-1} led to peak supersaturations of 0.3%, 0.6%, and 1.0%, respectively. With observed cloud base updraft velocities for NAMMA on the order of 3 m s^{-1}, supersaturations may peak near 0.1%, especially given that there were high concentrations of dust particles that acted as CCN near cloud base (Twohy et al. 2009). Therefore, activation of new cloud droplets was likely in the stronger updraft regions sampled during our field campaigns. This would account for the trend of increasing IWC/LWC with height.

The model results indicate that accretional growth rates are small relative to the rates of ice diffusional growth only when the updrafts are weak and for the low initial LWCs of 0.1 g m^{-3} that are used. This finding indicates that the results of the Heymsfield et al. (2005) study that considered only diffusional growth of the large ice are valid for the weaker updraft regions, where there is little if any liquid water. For such situations, we reiterate a process that Heymsfield et al. (2005) referred to as delayed homogeneous ice nucleation. With homogeneous nucleation, droplets are lofted to about −38°C and freeze homogeneously. Sometimes pre-existing ice or weak updrafts can limit the maximum RH to less than 100% and prevent droplet lofting and/or new droplet activation. With relative humidities above 75% or 80%, however, CCN not already incorporated in drops will absorb moisture and thus swell. Delayed homogeneous nucleation of these small solution droplets will eventually occur at a temperature somewhere below −38°C because the homogeneous nucleation rate continues to increase with decreasing temperature. In other words, even if droplets are not produced, homogeneous nucleation can occur at a lower temperature.

5. Summary and conclusions

This study has characterized the microphysical properties of updraft and neighboring regions at temperatures from −20° to −60°C in low-latitude clouds, 25°N to 11°S, emphasizing those regions where droplets and small ice particles are present in abundance. Data from

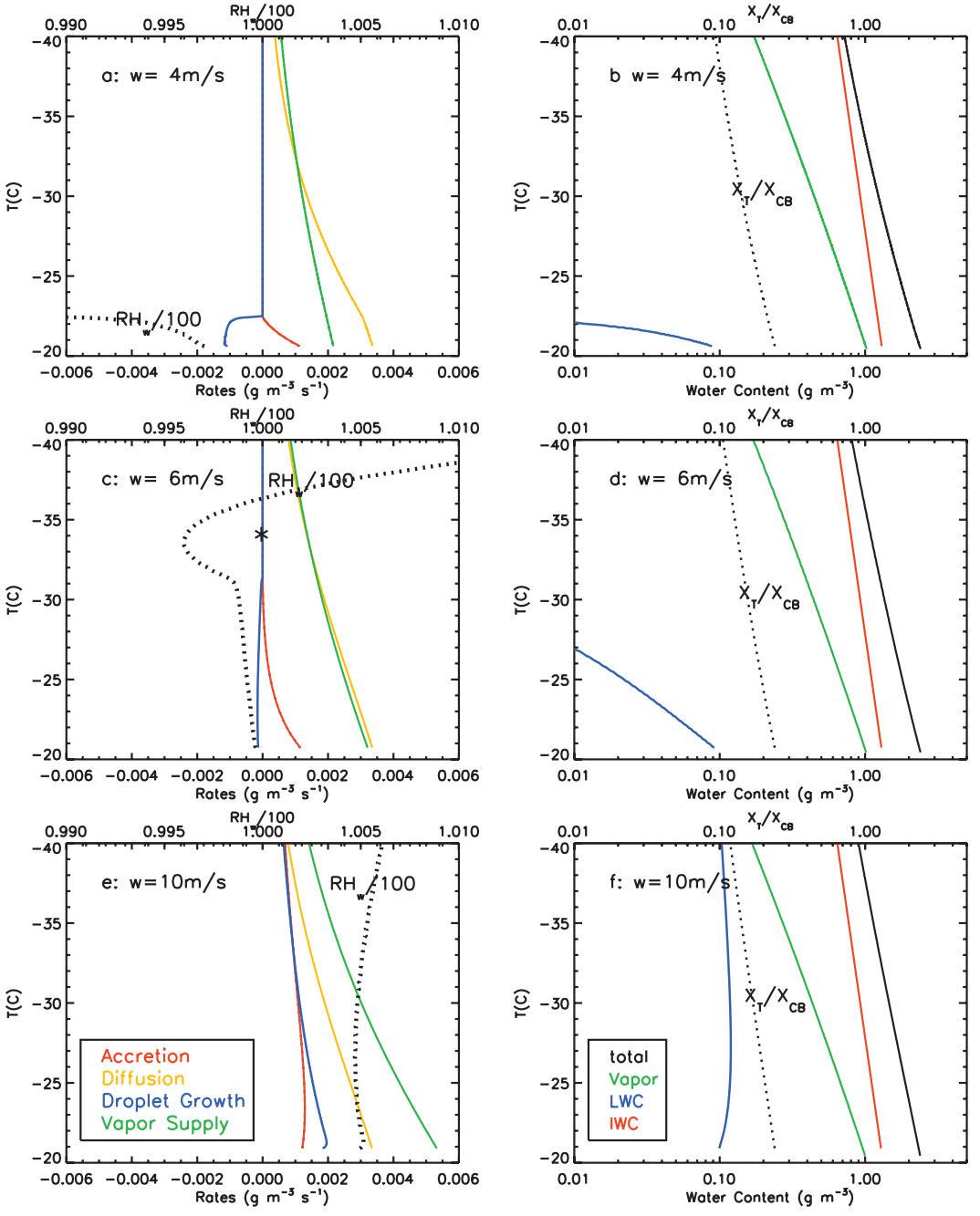

FIG. 15. (left) Beginning with an LWC = 0.1 g m^{-3} and an IWC = 1.32 g m^{-3} at −20°C, model calculations of the change in the partitioning of the water phases in updrafts as a function of temperature with increasing vertical velocity. Also shown is the ratio of the total water mixing ratio divided by the mixing ratio at cloud base assuming a cloud base temperature of 22°C and pressure of 931 hPa. (right) The rates of change of each water substance. The slope of the graupel PSD is taken to be 50 cm^{-1} and the density as 0.2 g cm^{-1}.

six maritime field campaigns and one nonmaritime campaign were used to investigate the fate of droplets lofted in the updrafts through this temperature range.

Our analysis depends on data from particle probes that were originally designed to measure the concentrations of droplets ranging in size from 3 μm to about 50 μm. Measurements from these probes are unreliable because large particles that shatter on the leading surfaces of these probes generate artifacts in the data. We therefore have developed methods to mitigate errors

in the measurement of the concentrations of small particles due to shattering. Had reliable measurements of small particles been available, our restrictive criteria for identifying the presence of small particles would have been unnecessary and many more occurrences of small particles, especially for relatively low concentrations, would have been identified. Additional data from probes designed to measure particles from 100 μm to above 1 cm, sensitive detectors of liquid water, accurate water vapor hygrometers, and lidar data are used in the study.

Of the more than 70 000 5-s periods or 50 000 km of horizontal path lengths examined in cloudy regions at temperatures −20°C and below, our analysis has reliably identified more than 1000 periods containing concentrations of true small particles at temperatures from −20° to −60°C. About 60% of these points are in updrafts, some as vigorous as 25 m s^{-1}. Within this temperature range, we have characterized the concentrations of small particles, derived the ice water content and cross-sectional areas in small and large particles, and derived the effective diameters and the properties of the size distributions in large particles and their mass-weighted fall speeds. We also estimated the fraction of the cloud base water vapor that reaches temperature levels from −20° to −60°C.

Within the updrafts identified as containing small particles, the median value of the concentrations of particles 3–50 μm is about 30 cm^{-3}; and for temperatures −40°C and below, it is about 40 cm^{-3}. By far the highest concentrations of droplets and homogeneously nucleated ice are found in the updrafts of NAMMA clouds sampled off the west coast of Africa, reaching 300 cm^{-3}. These high concentrations can be largely attributed to dust as ascertained from the aerosol residuals left from evaporated ice particles in the CVI probe (C. Twohy 2009, unpublished manuscript). There is on average a factor of 4 decrease in the IWC in large (>50 μm) ice particles between the −20° and −60°C levels. That, coupled with the finding that peak ice particle sizes decrease upward, indicates appreciable fallout of condensate to temperatures of −20°C level and below. Our observations indicate that only about 20% of the vapor flowing into cloud base makes its way up to the −20°C level. The ice water content and volume extinction coefficient in small particles (3–50 μm) increases through this temperature range, supplying a much larger contribution to the volume extinction coefficient, and thus to the albedo, than the large ice at the lower temperatures. For that reason, the role of small particles must be considered in climate models.

A 1D parcel model based on our observed vertical profiles of ice water content and exponential size distributions fitted to measured values was developed to examine the fate of cloud water as it is lofted from the −20°C to −38°C levels where water droplets will homogeneously freeze. For updraft velocities above about 7 m s^{-1}, the rate of condensation of vapor due to cooling—releasing up to a net of 0.88 g m^{-3} to ice growth and liquid water between −20° and −40°C—is sufficient to overcome the effects of accretional and diffusional growth of the large ice. Ice diffusional growth dominates over accretional growth. For that reason, the detailed modeling results reported in Heymsfield et al. (2005), which did not consider ice accretional growth in the updrafts of a modeled low-latitude vigorous convective cell, are useful. Three complementary effects promote the homogeneous ice nucleation process as inferred from observations and the model: first, the 80% of loss of total water from cloud base to the −20°C level, much of which is the result of fallout of the large ice particles; second, the additional halving of the condensed water content to the homogeneous nucleation level; and third, the corresponding increase in the vertical velocities in the intense updraft cores. For updrafts weaker than 7 m s^{-1}, the process of homogeneous ice nucleation of solution droplets—delayed homogeneous ice nucleation (Heymsfield et al. 2005)—must still be considered a viable process.

Large water supersaturations were reached for updraft velocities of 7 m s^{-1} in our model as a result of our decision not to include new droplet activation. Our observations do point to new droplet activation in the updrafts, especially for the NAMMA cases. The concentrations of small particles (as expressed in cm^{-3}) should have decreased by about a factor of 3 from cloud base to the −20°C level because of parcel expansion alone and even more through drop coalescence and collection by the large ice. Concentrations just above cloud base with dust in the boundary layer were at most a factor of 2 larger. Observations and cloud-resolving simulations suggest that updrafts entrain appreciable environmental air in the first 2 km or so above cloud base (e.g., Zipser 2003; Murata and Ueno 2005; Fierro et al. 2009). Lidar observations showed that the boundary layer adjacent to the most vigorous cell sampled during NAMMA was about 4.5 km deep and was filled with Saharan dust aerosol. Cloud base height was about 0.5 km. A rich source of dust CCN (Twohy et al. 2009) could readily have been entrained into the updrafts above cloud base. Because they would not have gone through the droplet activation process, they would constitute a potentially large concentration that could activate at relatively low supersaturations in the mid-cloud levels. These could have an important role in the homogeneous nucleation process in the NAMMA and other vigorous maritime convective cores.

Acknowledgments. The authors wish to thank Charlie Knight, Simone Tanelli, Hugh Morrison, Earle Williams, Steve Rutledge, Sandra Yuter, and Peggy Lemone for valuable discussions. The authors also wish to thank Syed Ismail, Glenn Diskin, and Cynthia Twohy for the valuable data they contributed. Editorial assistance was provided by Meg Miller. This research was supported by NASA through Grants NNX06AC67G (Ramesh Kakar, Project Manager) and NNX07AL11G (Hal Maring, Project Manager).

APPENDIX A

Identification of Small Particles (3–50 μm)

Wind tunnel studies have shown that ice particles that impact the leading surfaces of cloud particle probes shatter (W. Strapp and A. Korolev 2008, personal communication). Some fragments have a trajectory that allows them to ricochet back into the airstream. These fragments eventually lose their upstream momentum and are swept downstream. Those with ideal trajectories pass through the probes' sensing area and are sampled as would-be true particles.

Heymsfield (2007) showed that in ice clouds the following empirical relationships represent the shattering effect:

$$\mathrm{IWC}_s = \mathrm{IWC}_{\mathrm{true}} + c_m \mathrm{IWC}_{\mathrm{2D}}, \tag{A1}$$

where IWC_s is the IWC derived by assuming that all particles measured by the small-particle probes are solid ice spheres, $\mathrm{IWC}_{\mathrm{true}}$ is the actual IWC contained in small particle sizes, and c_m is the ''shattering coefficient'', empirically derived. If the small particles are true liquid droplets but large ice is present, then $\mathrm{LWC}_{\mathrm{true}}$ replaces $\mathrm{IWC}_{\mathrm{true}}$. From Eq. (A1), because

$$\mathrm{IWC}_{\mathrm{2D}} = \frac{1}{c_m}(\mathrm{IWC}_s - \mathrm{IWC}_{\mathrm{true}}), \tag{A2}$$

where scaling of IWC_s by $1/c_m$ when few true small particles are present should approximately reproduce the values of $\mathrm{IWC}_{\mathrm{2D}}$.

The CVI probe measures the condensed water content for small and large particles together. Equations (A1) and (A2) would apply when $\mathrm{IWC}_{\mathrm{true}}$ or $\mathrm{LWC}_{\mathrm{true}}$ are small relative to $\mathrm{IWC}_{\mathrm{2D}}$, that is, $s_m\mathrm{IWC}_s \approx \mathrm{CWC}$. In liquid water only regions, then $\mathrm{LWC}_s = \mathrm{CWC}$. The IWC_s–CWC relationship would break down when there is appreciable small ice or droplets together with large ice (e.g., mixed-phase regions)—that is, because $\mathrm{IWC}_{\mathrm{true}}$ would not be subtracted from IWC_s, Eq. (A2) would produce a value of $\mathrm{IWC}_{\mathrm{2D}}$ that would be an overestimate of that derived from the 2D probes.

Heymsfield (2007) also found that the total cross-sectional areas in small particles (A_s) as derived by assuming that all small particles are spheres and in large particles as derived from the 2D particle images (A_{2D}) are related by

$$A_s = A_{\mathrm{true}} + \frac{1}{c_a} A_{\mathrm{2D}}. \tag{A3}$$

Therefore, a good estimate of A_{2D} should be derived from

$$A_{\mathrm{2D}} = \frac{1}{(A_s - A_{\mathrm{true}})}. \tag{A4}$$

An evaluation of the methodology given by Eq. (A4) using data from the DLH hygrometer from NAMMA has been conducted. Besides measuring water vapor content, the hygrometer has been used to measure transmission at a wavelength of 1.3 microns over its 25-m open path distance. A paper reporting on the important results is in preparation. Heymsfield (2007) found the shattering coefficients in Eqs. (A1)–(A4) by fitting curves to scatterplots of IWC_s or A_s against IWC or A determined from the 2D probes, or from the CWC (the sum of the LWC and/or IWC) measured by the CVI in regions where there were evidently insignificant contributions from small particles. The values of the shattering coefficients were found to vary, depending on the type of probe used and its calibration, the probes' placement on the aircraft, and the aircraft true airspeed.

We use the methodology of Heymsfield (2007) to evaluate the presence of small particles in the clouds studied here. To illustrate the process, we scale the small-particle probe data using Eqs. (A2) and (A4). Figure A1a compares IWC_s to CWC from the CVI and $\mathrm{IWC}_{\mathrm{2D}}$ from C-F where temperatures were about −47°C. Here, CWC and $\mathrm{IWC}_{\mathrm{2D}}$ compare favorably, suggesting that our estimates of the crystal masses are quite accurate and that $\mathrm{IWC}_{\mathrm{true}}$ is likely quite small. Increasing IWC_s by $s_m = 5.6$ brings the IWC estimates from the FSSP in line with those measured by the CVI and estimated from the 2D probes. On the same flight, at a temperature of –5°C, there were regions of only liquid water as inferred from the RICE probe signal (see times given by symbols at the top of Fig. A1b) and where $\mathrm{IWC}_{\mathrm{2D}} \approx 0$ g m^3. Because such regions are dominated by or exclusively comprised of droplets and small drops smaller than several hundred microns, we set $\mathrm{IWC}_{\mathrm{2D}} = 0$ g m^{-3} and $s_m = 1.0$. For example, for the period 1928 to 1938 UTC, the LWC_s and $\mathrm{CWC}_{\mathrm{CVI}}$ have about the same values. Heymsfield (2007) concluded that for the

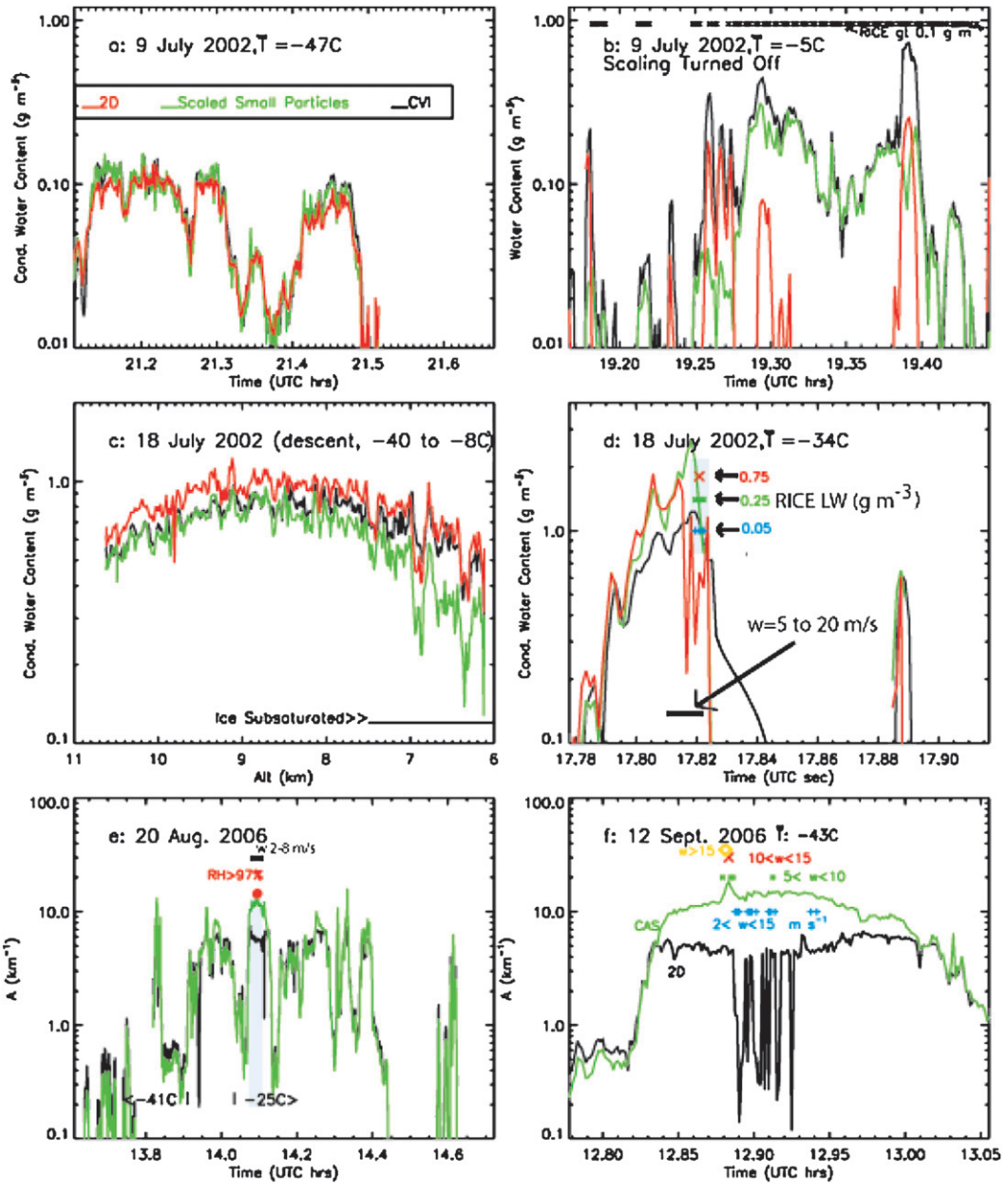

FIG. A1. In (a)–(d), measurements of CVI CWC (black) and also estimated from the PSDs in small (FSSP; green) and large (2D; red) sizes for two cases from C-F. The FSSP IWCs are scaled for shattering (see text). Scaling in (b) is set to 1.0 (no scaling) because most of the penetration is in liquid water (see times of RICE LW at top). Times of RICE LW are also shown in (b). (e),(f) The total area in small (CAS) and large (2D) particles for two NAMMA cases, respectively. The CAS LWCs are scaled (see text). Regions of high RH from a diode laser hygrometer and times of strong updrafts are shown. In (a)–(f), flight days and temperatures are shown.

mixed-phase periods (e.g., 1925 to 1938 UTC), Eq. (A2) gave the sum of the LWC in small particles and the shattering signature for the large ones.

On 18 July, also during C-F, a Lagrangian-type spiral descent was used to sample an anvil from near its top to base. Scaling of the IWC_s by a factor of 5.6 nearly matches CWC and IWC_{2D} (Fig. A1c) in the subsaturated region below 7 km. We presume that some of the shattered fragments experienced sublimation before they were sampled by the FSSP. Earlier on 18 July, a strong updraft was penetrated (Heymsfield et al. 2005; see also Fig. A1d). Scaling by a factor of $c_m = 5.6$ was appropriate in the ice regions on either side of the updraft core before 1780 and after 1788 UTC. The core contained

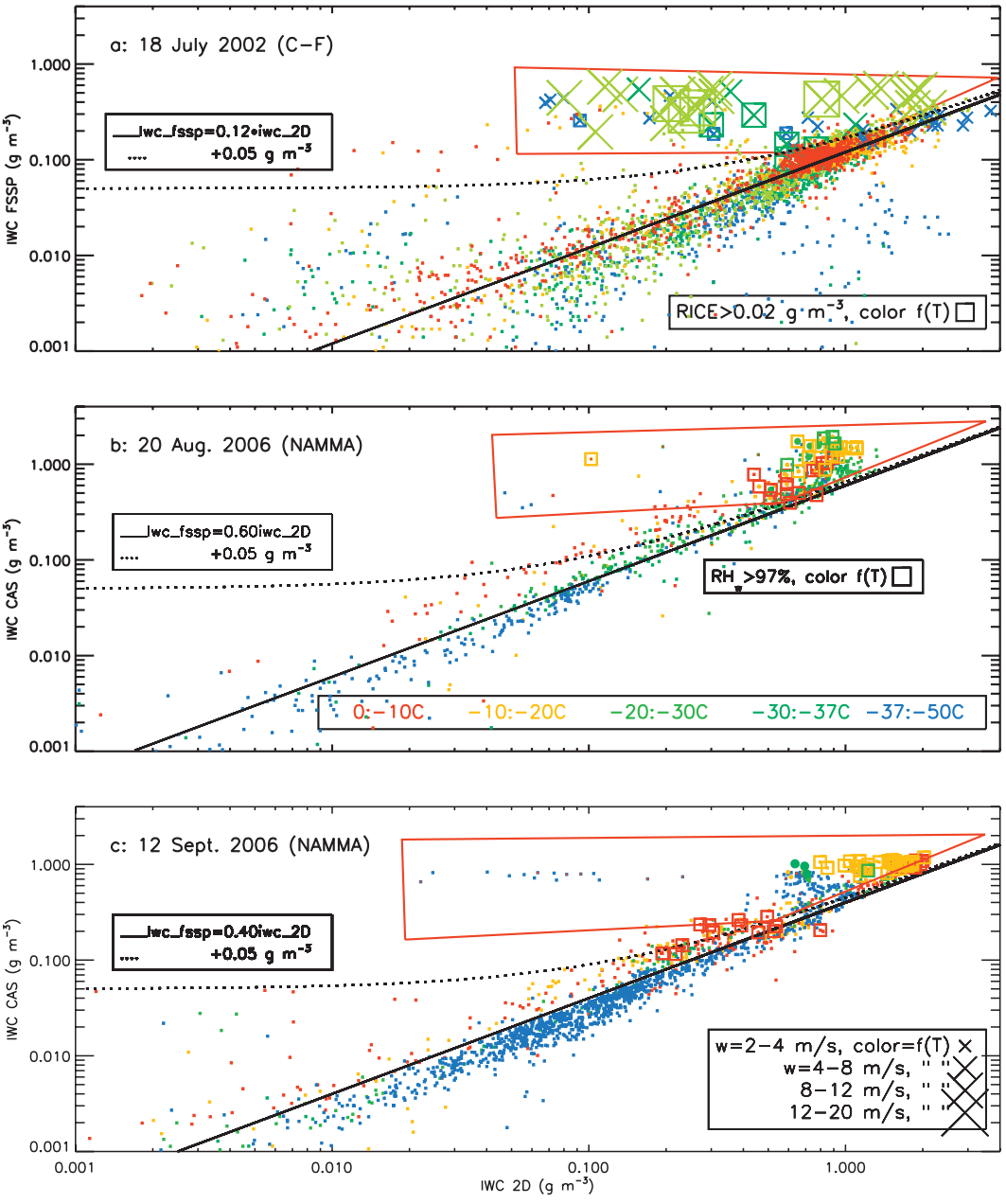

FIG. A2. Ice water content derived from 5-s average 2D and FSSP or CAS PSD for cases from (a) C-F and (b),(c) NAMMA. Solid line shows the fitted relationship between the IWC_{2D} and IWC_s, the slope of which is c_m [Eq. (A1)]. Dotted line shows what the IWC_{2D}–IWC_s relationship would look like with the addition of a "true" IWC of 0.05 g m^{-3} in small particles. The interactively drawn boxes show regions where true small particles are thought to be detected by the FSSP or CAS. Color coding shows the sampling temperature, and symbol size shows the vertical velocity. Regions of RICE LW and high RH are shown.

liquid water, and homogenous nucleation was identified in the updrafts higher up. The CVI probe was saturated (CWC_{CVI} above about 1 g m^{-3}) and could not be used. In the updraft core the IWC_{2D} values were low and scaling would not have produced the large values of IWC_s that were observed. We surmise that the value of IWC_s was the sum of a dominance of small cloud particles with some contribution from shattering by large ice.

We illustrate the relationship between A_s and A_{2D} for strong updraft cores penetrated on two days during NAMMA. On 20 August, scaling the A_s by a factor of 2.3 yields A_s values that are close to those of A_{2D} on

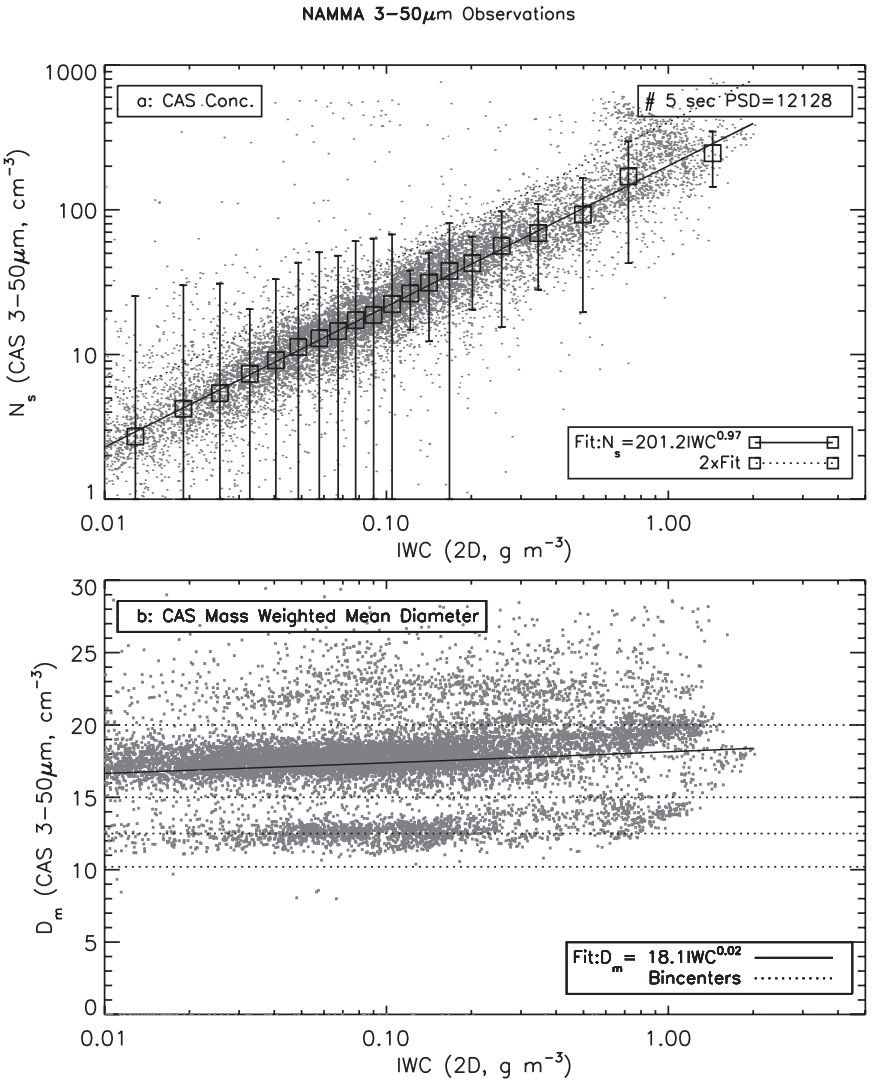

FIG. A3. Concentration N_t (3−50 μm) in diameter from the CAS as a function of IWC_{2D} from 13 NAMMA research flights. (a) Total number concentration. A curve $N_t = 2 \times 201.2IWC^{0.97}$, fitted to the data, and one that shows $N_t = 2 \times 201.2IWC^{0.97}$ to represent an envelope enclosing most points are shown. (b) Mass-weighted mean diameter. A linear curve fit to the data is plotted. The two groupings of points have to do with a calibration change for the last two NAMMA flights.

either side of the 8 m s^{-1} updraft core. In the core, where the relative humidities with respect to water are >97%, likely indicating the presence of droplets, scaling greatly overpredicts A_{2D} because in Eq. (A4) the A_{true} values are not subtracted. A broad region where scaling does not fit the observations with $s_a = 3.2$ was observed on 12 September in a region with vertical velocities ranging from 5 to 23 m s^{-1}. This was obviously a broad region with high concentrations of small particles, presumably lofted from below.

We now show that elevated concentrations of small particles affect the relationship between IWC_s and IWC_{2D}. In Fig. A2, linearity between IWC_s and IWC_{2D} is clearly noted. In Eq. (A1), $c_m = 0.12$ for the C-F case (Fig. A2a), 0.60 for the 20 August NAMMA case, and 0.40 for the 12 September NAMMA case. The curves representing the shattering signal are plotted in the panels. The dotted line in the panels shows what an IWC_{real} of 0.05 g m^{-3} would add to the shattering signal. In Fig. A2, there are points that fall well above the line representing shattering. These are contained within the boxed regions and occur within regions of strong updrafts. Liquid water detected from the RICE probe (Fig. A2a) and high RH from the diode laser hygrometer

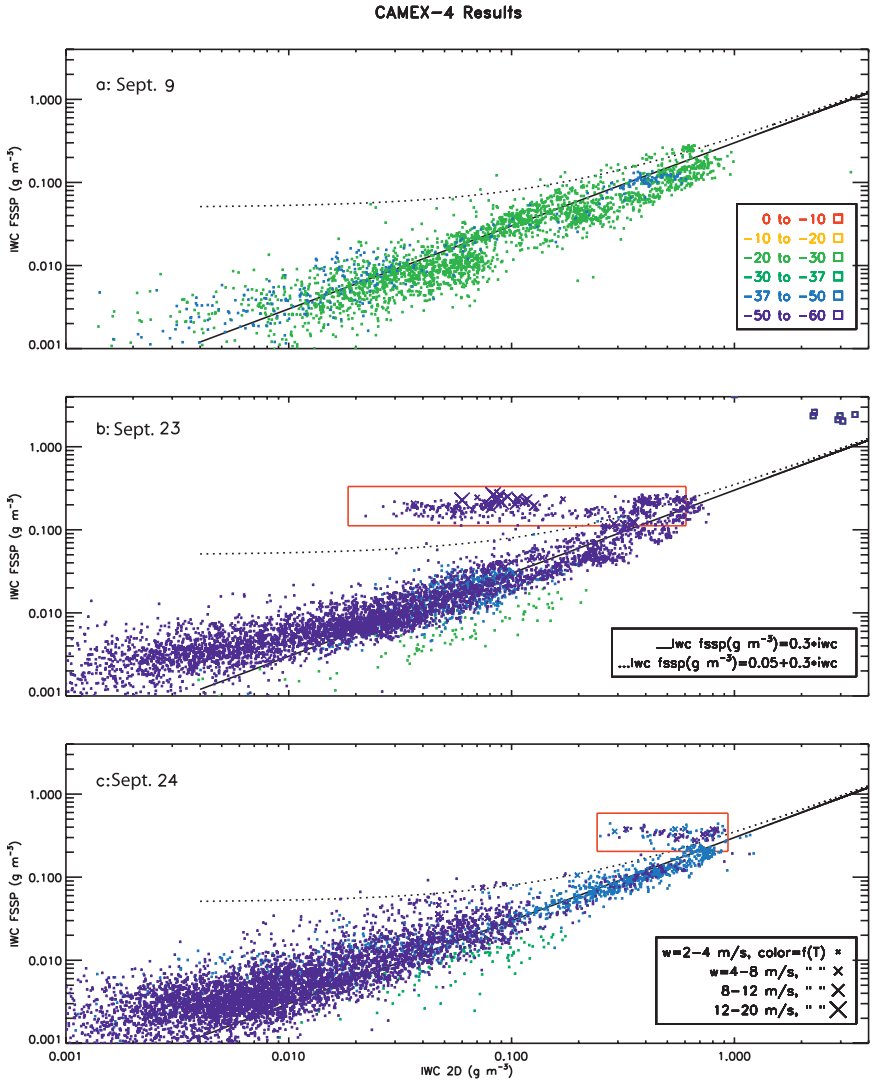

FIG. A4. As in Fig. A2, but for three flights during CAMEX-4.

(Figs. A2b,c) likely indicate the presence of liquid water. (No RICE liquid water measurements were available from NAMMA.) The amount of IWC_{true} is approximately given by the offset of IWC_s above the shattering line and comes to several tenths of a gram per cubic meter or more.

Why do we find the linear relationships as given by Eqs. (A1)–(A4)? Figure A3a compares N_s to IWC_{2D} for all of the points from 13 cases from NAMMA. As shown by the curve fit in the figure, the relationship is nearly linear. Figure A3b shows that the mass-weighted mean CAS diameters, D_m, are nearly constant with increasing IWC_{2D}. To a first approximation $IWC_s = \pi/6 N_s D_m^3$, so that substituting in the curve fits in Figs. A3a and A3b leads to $IWC_s = 0.63\ IWC^{1.03}$, close to the values of c_m that fit the two NAMMA cases in Fig. A2. We find the same explanation for the area relationship given by Eq. (A2) (not shown): $N_t \propto A^{0.97}$, $D_a \propto A_{2D}^{0.02}$, leading to $A_s \propto A_{2D}^{1.01}$.

The times of occurrence of numerous small droplets or homogeneously nucleated ice crystals have been identified for all cases from the field programs studied here by interactively identifying points that lay well above the shattering curve (e.g., boxed region, Figs. A2a–c). The concentrations of true small particles are quantified as follows. With reference to Fig. A3, an approximate upper limit to the concentrations produced by shattering is estimated to be 1.5 to 1.75 times the mean value on a plot of N_s versus IWC_{2D} (see Fig. A3a), depending on the field program. These concentrations are then subtracted from N_s. Note that there was a calibration shift downward by about 2 microns for the last two NAMMA flights, 9 and

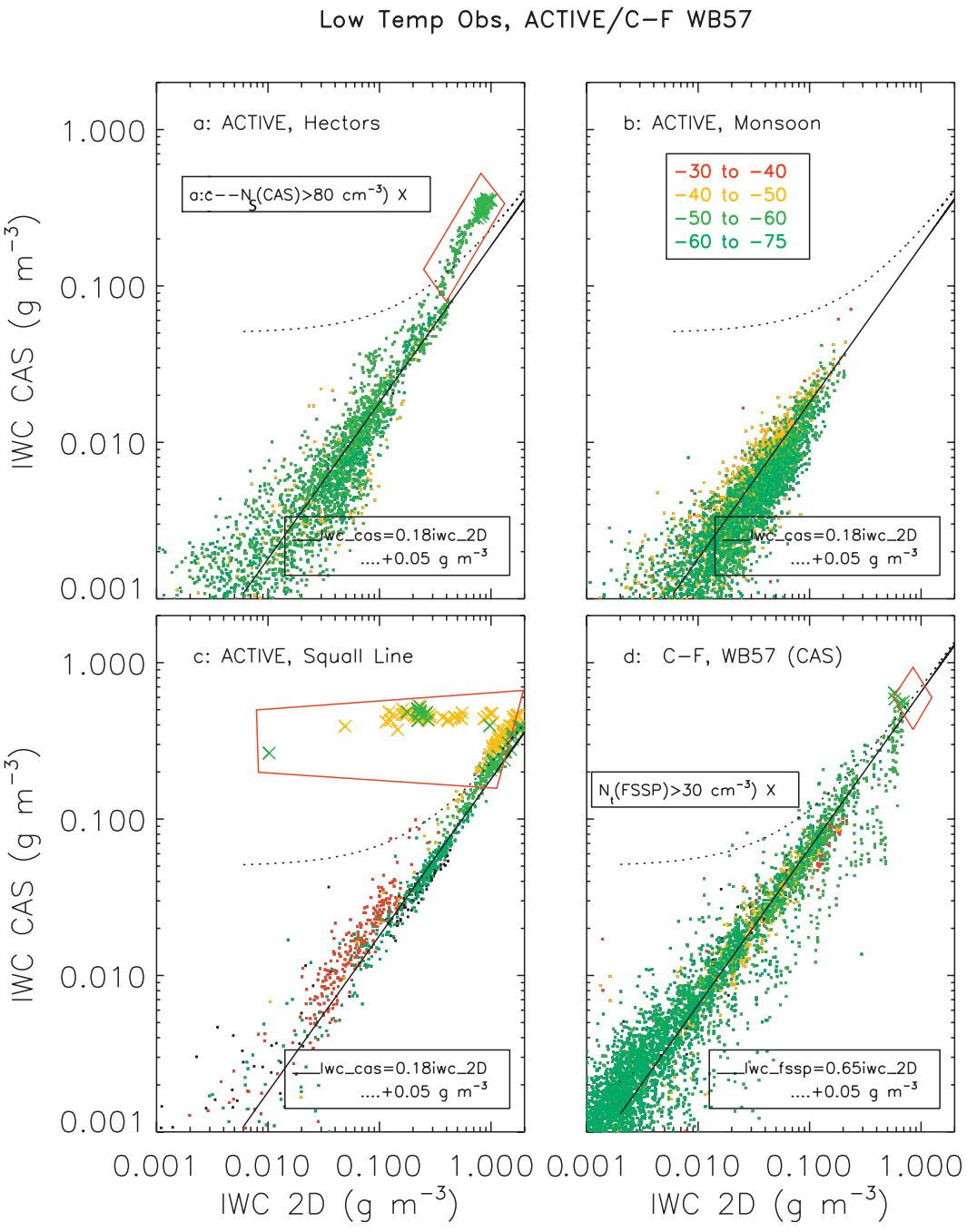

FIG. A5. (a)–(c) As in Fig. A2, but from the ACTIVE field program in (a) Hector clouds, (b) monsoon layer clouds, and (c) squall lines. (d) Data from the 29 July 2002 C-F WB57F case. Points denoted by × mark where the concentrations are relatively large and thus the likely high concentrations of true small particles.

12 September, which accounts for the two trends observed between CAS mass-weighted diameters and IWC. Because we have set the shattering envelope to be quite high, we may have missed periods of homogeneous nucleation.

We further establish confidence in the methods developed above for the remaining field programs. Figure A4 shows the relationship between IWC_s and IWC_{2D} for three of the cases from CAMEX-4. The characteristic signature of high concentrations of small particles is clearly identifiable within the boxed regions of Figs. A4b and A4c.

Figure A5 shows the relationship between IWC_s and IWC_{2D} for three of the cases from ACTIVE and a case

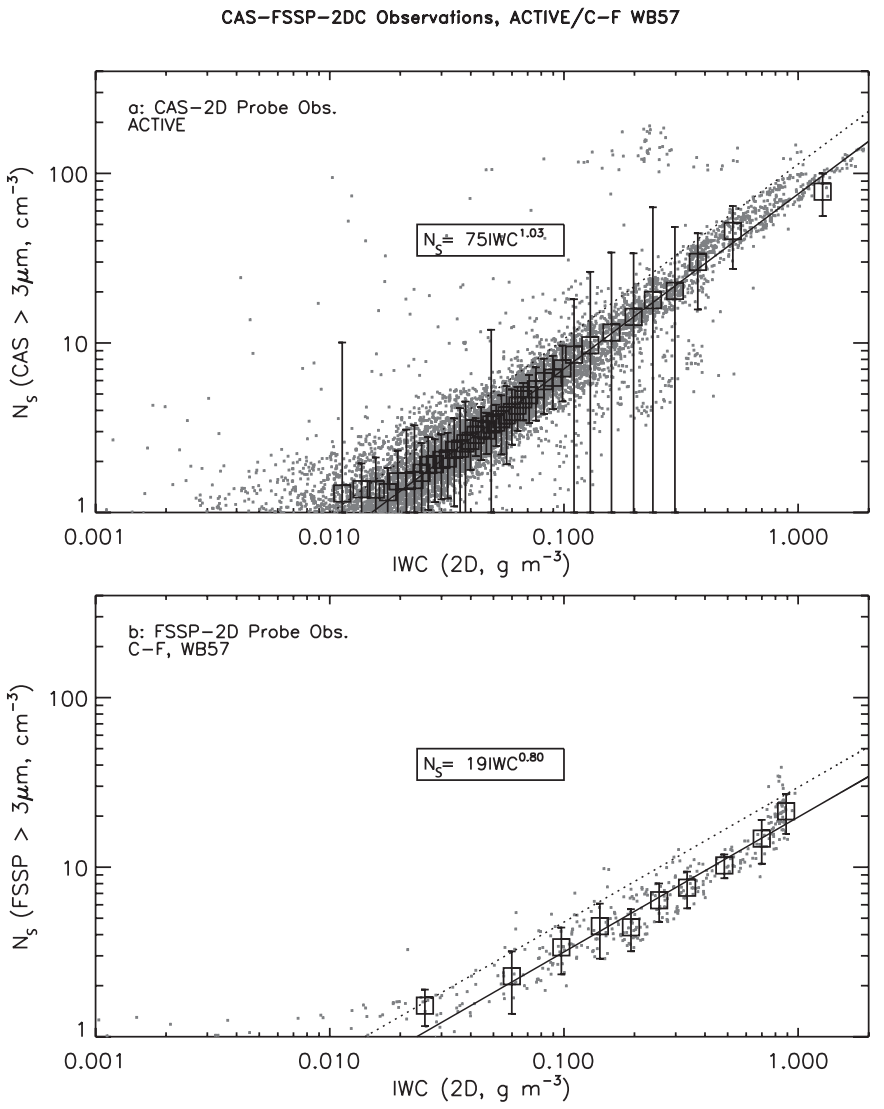

FIG. A6. As in Fig. A1, but for the (a) ACTIVE clouds and (b) all C-F cloud sampled by the WB57F.

from C-F that was sampled by the NASA WB57-F. The characteristic signature of high concentrations of small particles is clearly identifiable within the boxed regions of the figure. Linearity is found between N_s for CAS and IWC_{2D} (Fig. A6a); it is not found for the few data points associated with the C-F case (Fig. A6b), presumably because of the small sample size.

A single, well-defined relationship between IWC_s and IWC_{2D} is noted for temperatures 0°C and below for the composite of data from all three TRMM field campaigns (Fig. A7a). Most points where the (estimated) LWC from the RICE probe exceeded 0.02 g m^{-3} clearly fall above the envelope of the curve representing the majority of points. These are in most cases associated with updrafts >2 m s^{-1} (Fig. A7c). Few points at temperatures below −37°C lie above the envelope, suggesting that homogeneous nucleation was rare in these clouds.

APPENDIX B

Ice Particle Densities and Masses

The IWCs in large particles were derived from the 2D probe size distributions. Estimates of the ice particle masses, necessary for the IWC calculations, use the mass–dimensional relationships derived from the C-F observations, primarily from anvil and neighboring regions (Heymsfield et al. 2004). Bulk densities implied by the $m(D)$ relationship decrease from 0.91 to 0.10 to 0.023 g cm^{-3} as particle diameters increase from 100 μm

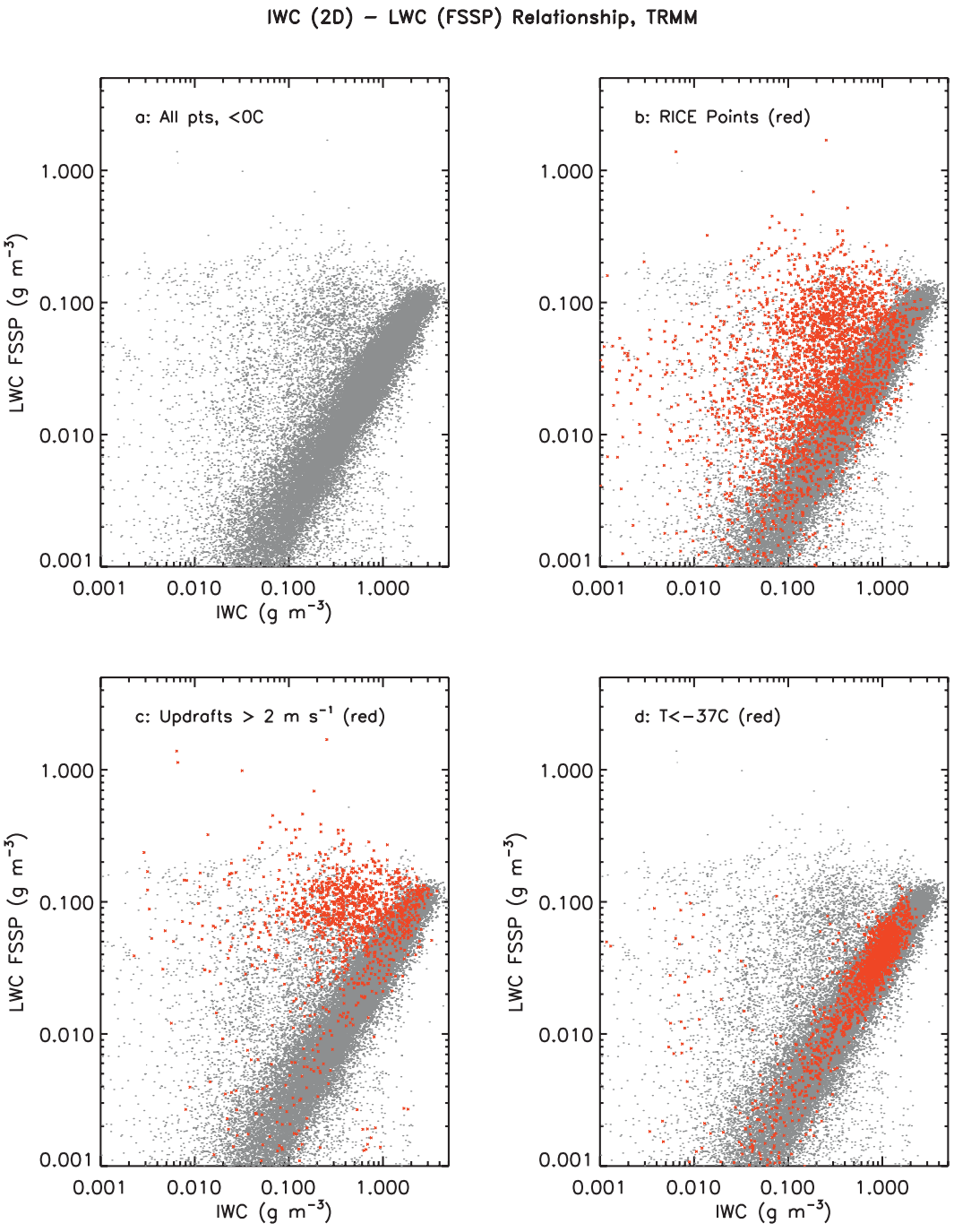

FIG. A7. As in Fig. A2, for the TRMM field campaigns. Regions of RICE LW and strong updrafts are identified by red symbols.

to 1 mm to 5 mm, respectively. Sizes 1 mm and below are the dominant contributors to the IWCs, even when much larger densities are prescribed for the particles above 1 mm.

The Heymsfield et al. (2004) relationship yields population-mean ice bulk densities (ρ_i) that fall in the range 0.09 to 0.37 g cm^{-3}, with a median value of $\overline{\rho}_i$ = 0.11 ± 0.07 g cm^{-3} for all periods. The ρ_i values are calculated from $\rho_i = \mathrm{IWC}_{2D}/(\Sigma V_i)$, where V_i is the spherical volume of a particle in size bin i times the number concentration in that size bin. The ρ_i and hence particle masses and IWC_{2D} may be underestimated because heavily rimed particles or graupel in updrafts could have higher densities. For the convective core on 18 July during

C-F, the large particles were graupel. Heymsfield et al. (2004) found that the $\overline{\rho}_i$ fell in the range 0.1 to 0.2 g cm^{-3}, with a mean value of about 0.15 g cm^{-3}, perhaps up to 50% larger than estimated by the $m(D)$ relationship.

We can use the CVI CWC measurements for C-F and NAMMA to evaluate our estimates of the IWC_{2D}. To remove or reduce periods when the CVI either was experiencing hysteresis or was saturated, the subset of CWCs from 0.1 to 1.0 g m^{-3} and where temperatures are 0°C and below are used. For the 18 July C-F case, which included data in vigorous convection, the median (mean) value of IWC_{2D}/CWC_{CVI} = 1.15 (1.14 ± 0.35); and for the 9 July C-F case when no liquid water was detected, IWC_{2D}/CWC_{CVI} = 0.87 (0.87 ± 0.11). For the 13 NAMMA cases, IWC_{2D}/CWC_{CVI} = 0.71 (0.76 ± 0.55). IWCs contributed by the small particles increase the ratios to IWC_{2D}/CWC_{CVI} = 0.93 (1.25 ± 1.54). These are obvious overestimates due to the contribution of shattered small particles. Nonetheless, there were numerous regions of supercooled liquid water that would have had significant contributions. If we further constrain the NAMMA dataset to temperatures −40°C and below where measurements for the 20 August and 12 September cases dominated the samples and there were significant contributions by the small particles, the ratio becomes IWC_{2D}/CWC_{CVI} = 0.74 (0.86 ± 0.67). Had we added in the contributions of the small particles, then $IWC_{2D} + IWC_s/CWC_{CVI}$ = 1.16 (1.36 ± 1.08). We are therefore not appreciably underestimating the particle masses, densities, and IWCs in most instances, with the exception of times in the convective updrafts where graupel densities would be higher than the $m(D)$ relationship would produce.

We evaluated the effect of varying ice particle masses and densities to assess uncertainties in our estimates of the ratio X_T/X_{CB}. Increasing the masses of the large particles by 50% increases the median value of the ratio from 0.13 to 0.17 for all cases combined (see dotted curve and legend, Fig. 13). Assuming the effective density of the large particles first to be 0.2 g cm^{-3} and then an unrealistically large value of 0.3 g cm^{-3} leads to fractions that increase to 0.20 and 0.29, respectively (see callout in Fig. 13). It is likely that the values of IWC_s are overestimates due to residual shattered particles in the PSDs from the small-particle probes; the masses may be overestimated if most of the small particles are pristine ice.

APPENDIX C

Ice Growth Model

Two versions of a model were developed to quantify the depletion of cloud water in a rising parcel of air. In both models, ice diffusional and accretional growth and droplet growth are offset by the rate of vapor condensation from parcel cooling during ascent. One version of the model assumes that the total water mixing ratio is conserved during vertical movement, whereas the second accounts for the observed decrease in total water substance with height (Fig. 8). Vertical velocities were taken to be constant with height.

The total water mixing ratio of a parcel of air is given by

$$X_T = X_v + X_l + X_i, \tag{C1}$$

where X_v, X_l, and X_i are the mixing ratios of vapor, liquid, and ice.

With time (t),

$$\frac{dX_l}{dt} = \frac{dX_T}{dt} - \frac{dX_v}{dt} - \frac{dX_i}{dt}. \tag{C2}$$

Air temperatures, pressures, and densities were derived assuming moist adiabatic ascent from the cloud-base temperature and height (section 3) through to the −40°C level. Initially at the −20°C level, a parcel was assumed to be at saturation with respect to water.

The ice mass growth rate dX_i/dt is the sum of the accretional rate dm_a/dt and the diffusional rate dm_d/dt summed for all ice particles, normalized by the air density. The accretional rate is

$$\frac{dm_a}{dt} = \mathrm{LWC}\sum_{D_0}^{D_{\max}} E(D)A(D)V_t(D)\,dD, \tag{C3}$$

where and $A(D)$ is the cross-sectional areas of the ice particle collectors. Equation (C3) is given in summation rather than integral form from some minimum diameter D_0 to a maximum $D_{\max}$ because we use discrete bins. For simplicity, the collection efficiency E is taken to be unity [see Heymsfield 1983 for $E(D)$ values]. Terminal velocities V_t are for graupel, as in Mitchell and Heymsfield (2005). The particles are assumed to have a circular cross-sectional area, and the densities of all particles are prescribed as ρ_i = 0.2 g cm^{-3}. The diffusional growth rate of ice is taken to be

$$\frac{dm_i}{dt} = 4\pi G_i' S_i \sum_{D_0}^{D_{\max}} CF, \tag{C4}$$

where S_i is the supersaturation with respect to ice based on the ambient relative humidity. The shape factor $C = D/2$ is that for spheres, and the ventilation coefficient F is given by Hall and Pruppacher (1976).

The droplet growth rate dm_w/dt takes on the form given by Eq. (C4), with G_w' replacing G_i' and the saturation ratio S-1 replacing S_i. The ventilation coefficient is taken to be 1.0. Droplets increase or decrease their

diameter assuming spheres of water density. The decrease in the saturation vapor density during one model time step ($t = 1$ s, or from 4 to 10 m in the vertical) was made available to the large ice to grow by accretion and diffusion and to the droplets to grow or evaporate.

In model 1, dX_I/dt was derived assuming conservation of total water substance; dX_T/dt in Eq. (C2) is 0. The PSDs were taken to be exponentials, with an initial slope $\lambda = 50$ cm^{-1}. At $t = 0$ s, where the temperature was -20°C, the concentrations were derived in 100 equally spaced size bins. The initial value of $D_{\max}$ was specified according to the equation given for $D_{\max}f(T)$ in Fig. 9C, which is 0.62 cm at -20°C. The initial IWC and assumed ρ_i gave N_0 for the exponential PSD. Droplets were monodisperse in size, with a diameter of 10 μm. Their initial number concentration was specified from the LWC.

The large ice first depleted cloud water due to accretion and cloud vapor due to diffusional growth. The droplets grew or evaporated based on the ambient (water) saturation ratio. The amount of condensate liberated from the decrease in the saturation mixing ratio during one model time step ($t = 1$ s) was taken up by the droplets. The condensate produced above the amount taken away by the growing droplets was added to the ambient water vapor, whereas if the condensate was below that amount it was subtracted. The excess vapor remaining in that time step was added to the liquid water mixing ratio. It was then accreted onto the growing ice with a rate given by Eq. (C3). Ice particles increased their size by accretion, with an assumed density of 0.2 g cm^{-3}, and by diffusion with a density of 0.91 g cm^{-3}. Droplets increased their size based on the growth rate.

In model 2, the IWC in large particles was specified as a function of temperature based on the averages from the observations (Fig. 7d), $\mathrm{IWC_{2D}} = 2.74e^{0.036T(°C)}$. The $\lambda = 50$ cm^{-1}, and for the given $\mathrm{IWC_{2D}}$ at each model time step, N_0 could be derived. The large ice grew by accretion and diffusion, less the amount of water vapor condensed during the time step. Any excess of condensed water vapor was added to the supersaturation with respect to water and then subtracted by the growth of the droplets. The IWC above the amount given by $\mathrm{IWC_{2D}}(T)$ at the given temperature due to growth of the graupel was removed from the parcel. The maximum diameter of each PSD was specified from the temperature using the equation given in Fig. 14c. The number of size bins was taken to be 100, equally spaced. Other details follow those given for model 1.

REFERENCES

Anderson, N. F., C. A. Grainger, and J. L. Stith, 2005: Characteristics of strong updrafts in precipitation systems over the central tropical Pacific Ocean and in the Amazon. *J. Appl. Meteor.,* **44,** 731–738.

Black, R. A., and J. Hallett, 1986: Observations of the distribution of ice in hurricanes. *J. Atmos. Sci.,* **43,** 802–822.

——, and ——, 1999: Electrification of the hurricane. *J. Atmos. Sci.,* **56,** 2004–2028.

——, H. B. Bluestein, and M. L. Black, 1994: Unusually strong vertical motions in a Caribbean hurricane. *Mon. Wea. Rev.,* **122,** 2722–2739.

DeMott, P. J., K. Sassen, M. R. Poellot, D. Baumgardner, D. C. Rogers, S. D. Brooks, A. J. Prenni, and S. M. Kreidenweis, 2003: African dust aerosols as atmospheric ice nuclei. *Geophys. Res. Lett.,* **30,** 1732, doi:10.1029/2003GL017410.

Dunion, J. P., and C. S. Velden, 2004: The impact of the Saharan air layer on Atlantic tropical cyclone activity. *Bull. Amer. Meteor. Soc.,* **85,** 353–365.

Evan, A. T., J. Dunion, J. Foley, A. Heidinger, and C. Velden, 2006: New evidence for a relationship between Atlantic tropical cyclone activity and African dust outbreaks. *Geophys. Res. Lett.,* **33,** L19813, doi:10.1029/2006GL026408.

Field, P. R., A. J. Heymsfield, and A. Bansemer, 2006: Shattering and particle interarrival times measured by optical array probes in ice clouds. *J. Atmos. Oceanic Technol.,* **23,** 1357–1371.

Fierro, A. O., J. M. Simpson, M. A. LeMone, J. M. Straka, and B. F. Smull, 2009: On how hot towers fuel the Hadley cell: An observational and modeling study of line-organized convection in the equatorial trough from TOGA COARE. *J. Atmos. Sci.,* **66,** 2730–2746.

Fridlind, A., and Coauthors, 2004: Evidence for the predominance of mid-tropospheric aerosols as subtropical anvil cloud nuclei. *Science,* **304,** 718–722.

Hall, W. D., and H. R. Pruppacher, 1976: The survival of ice particles falling from cirrus clouds in subsaturated air. *J. Atmos. Sci.,* **33,** 1995–2006.

Hallett, J., and S. C. Mossop, 1974: Production of secondary ice particles during the riming process. *Nature,* **249,** 26–28.

Hartmann, D. L., M. E. Ockert-Bell, and M. L. Michelsen, 1992: The effect of cloud type on earth's energy balance: Global analysis. *J. Climate,* **5,** 1281–1304.

Heymsfield, A. J., 1983: A technique for investigating graupel and hail development. *J. Climate Appl. Meteor.,* **22,** 1143–1160.

——, 2007: On measurements of small ice particles in clouds. *Geophys. Res. Lett.,* **34,** L23812, doi:10.1029/2007GL030951.

——, A. Bansemer, C. G. Schmitt, C. Twohy, and M. R. Poellet, 2004: Effective ice particle densities derived from aircraft data. *J. Atmos. Sci.,* **61,** 982–1003.

——, L. M. Miloshevich, C. Schmitt, A. Bansemer, C. Twohy, M. R. Poellot, A. Fridlind, and H. Gerber, 2005: Homogeneous ice nucleation in subtropical and tropical convection and its influence on cirrus anvil microphysics. *J. Atmos. Sci.,* **62,** 41–64.

——, A. Bansemer, S. L. Durden, R. L. Herman, and T. P. Bui, 2006: Ice microphysics observations in Hurricane Humberto: Comparison with non-hurricane-generated ice cloud layers. *J. Atmos. Sci.,* **63,** 288–308.

——, P. Field, and A. Bansemer, 2008: Exponential size distributions for snow. *J. Atmos. Sci.,* **65,** 4017–4031.

Heymsfield, G. M., L. Tian, A. J. Heymsfield, and L. Li, 2010: Characteristics of deep tropical and subtropical convection from nadir-viewing high-altitude airborne Doppler radar. *J. Atmos. Sci.,* in press.

Koop, T., B. Luo, A. Tsias, and T. Peter, 2000: Water activity as the determinant for homogeneous ice nucleation in aqueous solutions. *Nature,* **406,** 611–614.

Lucas, C., E. J. Zipser, and M. A. Lemone, 1994: Vertical velocity in oceanic convection off tropical Australia. *J. Atmos. Sci.,* **51,** 3183–3193.

Marks, F. D., Jr., and R. A. Houze Jr., 1984: Airborne Doppler radar observations in Hurricane Debby. *Bull. Amer. Meteor. Soc.,* **65,** 569–582.

Mazin, I. P., A. V. Korolev, A. J. Heymsfield, G. A. Isaac, and S. G. Cober, 2001: Thermodynamics of icing cylinder for measurements of liquid water content in supercooled clouds. *J. Atmos. Oceanic Technol.,* **18,** 543–558.

May, P. T., and D. K. Rajopadhyaya, 1996: Wind profiler observations of vertical motion and precipitation microphysics of a tropical squall line. *Mon. Wea. Rev.,* **124,** 621–633.

Meyers, M. P., P. J. DeMott, and W. R. Cotton, 1992: New primary ice-nucleation parameterizations in an explicit cloud model. *J. Appl. Meteor.,* **31,** 708–721.

Mitchell, D. L., and A. J. Heymsfield, 2005: Refinements in the treatment of ice particle terminal velocities, highlighting aggregates. *J. Atmos. Sci.,* **62,** 1637–1644.

Murata, A., and M. Ueno, 2005: The vertical profile of entrainment rate simulated by a cloud-resolving model and application to a cumulus parameterization. *J. Meteor. Soc. Japan,* **83,** 745–770.

Rosenfeld, D., and W. L. Woodley, 2000: Deep convective clouds with sustained supercooled liquid water down to 37.5°C. *Nature,* **405,** 440–442.

Rossow, W. B., and R. A. Schiffer, 1999: Advances in understanding clouds from ISCCP. *Bull. Amer. Meteor. Soc.,* **80,** 2261–2287.

Samsury, C. E., and E. J. Zipser, 1995: Secondary wind maxima in hurricanes: Airflow and relationship to rainbands. *Mon. Wea. Rev.,* **123,** 3502–3517.

Stith, J. L., J. A. Hagerty, A. J. Heymsfield, and C. A. Grainger, 2004: Microphysical characteristics of tropical updrafts in clean conditions. *J. Appl. Meteor.,* **43,** 779–794.

Twohy, C. H., and Coauthors, 2009: Saharan dust particles nucleate droplets in Eastern Atlantic clouds. *Geophys. Res. Lett.,* **36,** L01807, doi:10.1029/2008GL035846.

Vaughan, G., C. Schiller, A. R. MacKenzie, K. Bower, T. Peter, H. Schlager, N. R. P. Harries, and P. T. May, 2008: SCOUT-O3/ACTIVE: High-altitude aircraft measurements around deep tropical convection. *Bull. Amer. Meteor. Soc.,* **89,** 647–662.

Wong, S., and A. E. Dessler, 2005: Suppression of deep convection over the tropical North Atlantic by the Saharan Air Layer. *Geophys. Res. Lett.,* **32,** L09808, doi:10.1029/2004GL022295.

Zipser, E. J., 2003: Some views on ''Hot Towers'' after 50 years of tropical field programs and two years of TRMM data. *Cloud Systems, Hurricanes, and the Tropical Rainfall Measuring Mission (TRMM)—A Tribute to Dr. Joanne Simpson, Meteor. Monogr.,* No. 51, Amer. Meteor. Soc., 49–58.

——, and M. A. LeMone, 1980: Cumulonimbus vertical velocity events in GATE. Part II: Synthesis and model core structure. *J. Atmos. Sci.,* **37,** 2458–2469.

——, R. J. Meitin, and M. A. LeMone, 1981: Mesoscale motion fields associated with a slowly moving GATE convective band. *J. Atmos. Sci.,* **38,** 1725–1750.

——, and Coauthors, 2009: The Saharan air layer and the fate of African easterly waves—NASA's AMMA field study of tropical cycogenesis. *Bull. Amer. Meteor. Soc.,* **90,** 1137–1156.